Response to reviewer #2

We thank the reviewer for his/her comments.

The authors have done substantial effort to improve the paper. They reduced the number of figures by 4, but increased the number of pages by 3, and hence, it still feels a little long. My main criticism is that the justification for this paper is not well expressed in the introduction. The only line in the introduction that touches on this is line 109 "Thus it is important to understand their shoaling dynamics." Can the authors write what the gaps are in the literature and how this paper addresses these gaps? I recommend publishing after shortening the paper and improving the justification.

Additional justification has been added to the introduction (see page 6). We have also gone through the paper and shortened it where possible. The paper has been reduced by about 1.5 pages in spite of the additional justification added to the introduction.

Minor points:

1. L121. English? Resolutions tests

   Fixed

2. L160-172. Is all this detail needed about the bathymetry? Removing it makes the paper shorter and less tedious to read. Rephrase it like h15 has a shallower bump and is steeper than h0.

   Most of the details of the bathymetry have been removed and slopes of different sections of them have been provided in figure 2.

3. L186. Please provide formulas for APE and KE.

   A formula for KE seems unnecessary. Regarding APE we have added "Here and throughout the APE is for waves in an infinite domain computed using the background density as the reference density (Lamb and Nguyen, 2009)".

4. L217. Define polarity

   Text now reads '... of either polarity (i.e., elevation or depression) ...'

5. L245. English? less that

   Corrected

6. L261. "and this is the environment it propagates in" I am not sure what the authors say here. I am also confused about the pedestal. Is it the square wave with elevated deep water density? In Figure 4e, is the first pedestal between 78 and 80 km and the second between 75 and 77 km? Can the authors also define it better? Maybe show in a Figure 4 what the pedestal is? Then phrases like which has now propagated into the pedestal and propagating on the wave pedestal may also become clear. What feature is propagating on the pedestal?

   The pedestal is the elevation wave that forms behind the leading depression. In Figure 4e it extends from the back of the leading depression at $x = 80$ km to

possibly $x \approx 74$ km (that is the single broad elevation that forms behind the leading waves is a single entity rather then different elevations formed behind each solitary wave). So, in Figure 4e the pedestal is between about 74 and 80 km with three trailing depressions, centred at $x = 74.5$, 75.2 and 77.5 km, imbedded in it. By "and this is the environment it propagates in" we mean that the trailing waves of depression are propagating in the stratification and background currents that are present in the pedestal. They don't 'know' about the stratification ahead of the leading depression. We have modified the text to clarify the extent of the pedestal and instead of refering to the 'first pedestal' we refer to the 'first part of the pedestal' as the former language is misleading..

7. L271. The wave speed equals the particle speed. Does this lead to overturns in the second pedestal?

   There are weak overturns as can be seen in the density profile for E2 in figure 6b. This has now been pointed out in the text.

8. L287. English? providing

   Fixed

9. L309. second box (or second wave for that matter in other places). The authors should include from the left or right to avoid confusion.

   Have changed text to "left box". We think that the meaning of 'second wave' is clear so have not made changes elsewhere in the text.

10. L311. I do not see downwelling because of the colorscale. Also I do not know at what depth. At the bump or higher in the water column?

    We have clarified that it is at the bottom and have referred to Figure 7b. In our figures it can be clearly seen so perhaps there was a problem with the conversion of the figure?

11. L387. You mean Figure 9d?

    Yes. Corrected (also in previous paragraph)

12. L417. Are the authors not precise enough? A solitary wave must scatter and reflect for (super)critical slopes?

    For steep slopes there must be some reflection however as the slope goes to zero the energy in the reflected wave goes to zero (according to weakly-nonlinear theory). In our simulations there is some reflected energy, mention of which has been made.

13. L424. Do the authors mean kinetic and available potential energy?

    Yes. Total energy. In weakly-nonlinear theory KE and APE are equal.

14. L425. What is the definition of mass and how is it different than APE?

    For a wave form $\eta(x,t)$ the mass is the integral of η while the energy, equally partitioned between kinetic and available potential energy, is proportional to the integral of η^2.

15. L473. except that the maximum currents occur in greater depths than do the maximum wave amplitudes This is always the case for a first mode wave, is it not? Maximum velocities at the surface and bottom and largest vertical wave amplitudes at zero crossings? You expect them to occur at different depths.

    We are referring to the maximum currents and wave amplitudes as a function of the water depth at the location of the wave (so equivalently as a function of time or horizontal position). As the wave shoals the wave amplitude changes and the maximum wave currents change. The maximum amplitude occurs at a different depth (i.e., at a different time and horizontal location) that do the maximum currents.

16. L523. English? vertically

    Fixed.

17. 544. Can the authors indicate what terms in the momentum equation are responsible for this difference in shoaling between model and theory?

    This difference is not a difference between model and theory here. Weakly-nonlinear theory (e.g., the shoaling KdV or Gardner equation) using the same bathymetry will predict wave deformations and fissioning similar to those seen in the model (see Lamb and Xiao, Ocean Modelling, 2014). The adiabatic curves by construction give the wave amplitudes and currents of solitary waves with fixed total energy. In reality the shoaling wave deforms and fissions so the leading waves are not exact solitary waves with energy equal to their initial energy. This occurs in both fully nonlinear simulations and in weakly-nonlinear models.

18. L672. English? various in stratification

    Sentence changed to ' 'Here we consider the sensitivity of the shoaling behavior to similar changes in the stratification."

19. L675. The shoaling waves in the simulations are internal tides because they are generated at Luzon strait by the surface tides. I guess the authors are referring to locally generated tidal internal waves? Please clarify. You may also say that undulations in stratification due to subtidal flow are missing in the simulations.

    We had locally generated internal tides in mind. Text modified.

20. L743. Use effects

    Fixed

21. L789. I would argue the opposite that if the bumps are a 3D phenomena, the flow could go around them and the response to the waves would be smaller than in a purely 2D bump (no variation along y), i.e. in a 2D model, you may see a stronger response.

    We agree. Text has been modified to read " As the bumps in the bathymetric transects are slices through three-dimensional features this implies that three-dimensionality of the bathymetry is likely an important factor in some locations,

particularly for the secondary waves that form during shoaling, though the effects of bumps may be mitigated in three-dimensions because the flow could go around them.".

22. L829. English? in out

    Fixed.

Manuscript prepared for Nonlin. Processes Geophys. Discuss.
with version 2014/07/29 7.12 Copernicus papers of the LaTeX class copernicus.cls.
Date: 16 March 2015

Two-dimensional numerical simulations of shoaling internal solitary waves at the ASIAEX site in the South China Sea

K. G. Lamb[1] **and A. Warn-Varnas**[2,*]

[1]Department of Applied Mathematics, University of Waterloo, Waterloo, Ontario, N2L 3G1, Canada
[2]Naval Research Laboratory, Stennis Space Center, MS 39539, USA
[*]retired

Correspondence to: K. G. Lamb (kglamb@uwaterloo.ca)

Abstract

The interaction of barotropic tides with Luzon Strait topography generates some of the world's largest internal solitary waves which eventually shoal and dissipate on the western side of the north South China Sea. Two-dimensional numerical simulations of the shoaling of a singe internal solitary wave at the site of the Asian Seas International Acoustic Experiment have been undertaken in order to investigate the sensitivity of the shoaling process to the stratification and the underlying bathymetry, and to explore the influence of rotation. The bulk of the simulations are inviscid however exploratory simulations using a vertical eddy-viscosity confined to a near bottom layer, along with a no-slip boundary condition, suggest that viscous effects may become important in water shallower than about 200 m. A shoaling solitary wave fissions into several waves. At depths of 200-300 m the front of the leading waves become nearly parallel to the bottom and develop a very steep back as has been observed. The leading waves are followed by waves of elevation (pedestals) that are conjugate to the waves of depression ahead and behind them. Horizontal resolutions of at least 50 m are required to simulate these well. Wave breaking was found to occur behind the second or third of the leading solitary waves, never at the back of the leading wave. Comparisons of the shoaling of waves started at depths of 1000 and 3000 m show significant differences and the shoaling waves can be significantly non-adiabatic even at depths greater than 2000 m. When waves reach a depth of 200 m their amplitudes can be more than 50% larger than the largest possible solitary wave at that depth. The shoaling behaviour is sensitive to the presence of small scale features in the bathymetry: a 200 m high bump at 700 m depth can result in the generation of many mode-two waves and of higher mode waves. Sensitivity to the stratification is considered by using three stratifications based on summer observations. They primarily differ in the depth of the thermocline. The generation of mode-two waves and the behaviour of the waves in shallow water is sensitive to this depth. Rotation affects the shoaling waves by reducing the amplitude of the leading waves via the radiation of long trailing inertia-gravity waves. The nonlinear-dispersive evolution of these inertia-gravity waves results in the formation of secondary mode-one wave packets.

1 Introduction

In the South China Sea (SCS) large internal solitary-like waves (ISWs) are frequently observed, ~~both~~ remotely via Synthetic Aperture Radar (SAR) and via in situ observations (Liu et al., 1998; Ramp et al., 2004; Klymak et al., 2006; Farmer et al., 2009; Li and Farmer, 2011). Analysis of ~~SAR surface signatures, and time series of current and temperature data at moorings,~~ these observations indicate that the ISWs are generated by barotropic tidal motion over the large sills in Luzon Strait and on the slope region of the northern boundary of the SCS (Liu et al., 1998; Hsu and Liu, 2000; Alford et al., 2010). Depressions generated in Luzon Strait propagate westwards across the deep South China Sea basin, where depths can exceed 4000 m, to the Asian Seas International Acoustic Experiment (ASIAEX) experimental site on the Chinese continental shelf. Nonlinear effects steepen these depressions until they disintegrate into ISWs of large amplitude, through frequency and amplitude dispersion. Zhao and Alford (2006) related the ISWs observed near Dongsha Island to tidal currents passing through Luzon Strait, finding that westward flow through the strait was responsible for the generation of the ISW packets however more recent studies have shown that eastwards currents are responsible for ~~generating the large westward propagating solitary waves (Buijsman et al., 2010) .~~ their generation (Buijsman et al., 2010) . Several numerical studies of ISW generation by tidal flow over the ridges in Luzon Strait have been conducted (Niwa and Hibiya, 2001, 2004; Warn-Varnas et al., 2010; Buijsman et al., 2010) .

Li and Farmer (2011) reported deep basin ISW amplitudes as large as 150 m with typical values being around 50 m. In situ measurements in the deep basin by Klymak et al. (2006) show ISWs with amplitudes as large as 170 m and phase speeds of 2.9 $\mathrm{m\,s^{-1}}$. During the joint Variations Around the Northern South China Sea (VANS) and Windy Island Soliton Experiment (WISE) (Yang et al., 2009), ISWs with amplitudes of up to 220 m and phase speeds of around 3.4 $\mathrm{m\,s^{-1}}$ were observed (Ramp, private communication). These measured amplitudes and phase speeds are among the largest observed anywhere, surpassing observed amplitudes of 90 m and phase speeds of 1.8 $\mathrm{m\,s^{-1}}$ in the Andaman and Sulu Seas (Osborne and Burch, 1980; Apel et al., 1985). ~~Because of the large amplitudes~~

of these waves they have been Their large amplitudes have made these waves the subject of many observational and numerical investigations. The dynamics of ISWs in the northern SCS was recently reviewed by Guo and Chen (2014).

Several numerical studies of ISW generation by tidal flow over the ridges in Luzon Strait have been conducted (Niwa and Hibiya, 2001, 2004; Warn-Varnas et al., 2010; Buijsman et al., 2010) elucidating the generation of ISWs in Luzon Strait and their subsequent westward propagation in the South China Sea. The structure of ISW wave trains in the SCS is variable with large amplitude wave trains separated by small amplitude wave trains (Ramp et al., 2004; Warn-Varnas et al., 2010; Buijsman et al., 2010; Vlasenko et al., 2012). Ramp et al. (2004) separated the wave packets observed at the ASIAEX site into a waves and b waves. The a waves arrived at regular 24 h intervals and were rank ordered, with the largest wave leading the wave packet. The weaker b waves were separated by approximately 25 h and were more irregular, with the largest wave usually in the middle of the packet. The formation of these wave packets is tied to the generation of the waves in Luzon Strait (Alford et al., 2010; Buijsman et al., 2010).

During the ASIAEX experiment, intensive measurements of shoaling ISW trains over the continental shelf off China were undertaken (Lynch et al., 2004; Duda et al., 2004; Orr and Mignerey, 2003; Ramp et al., 2004). Ramp et al. (2004) reported on observations from a series of moorings spanning depths of 350 to 72 m illustrating the evolution of these waves as they shoaled. At 350 m depth wave the waves were fairly symmetric with amplitudes ranged from 29 to 142 m (based on the displacement of the 24° isotherm). Their observations illustrated the evolution of these waves as they shoaled. At 350depth the waves were fairly symmetric. By the time they reached a depth of 200 m they had usually deformed significantly with a gently sloping front and a much steeper rear. Orr and Mignerey (2003) tracked a shoaling solitary wave ISW train with a towed conductivity, temperature, and depth sensor (CTD), observing the evolution of shoaling ISW trains from waves of depression to waves of elevation. Mode-two solitary-like waves were observed during the ASIAEX experiment (Orr and Mignerey, 2003) but not reported on in detail. Observations of a mode-two ISW

made during a pilot study for the ASIAEX experiment were reported on in Yang et al. (2004). Many mode-two solitary-like waves were observed at 350 m depth in a nearby region during the joint VANS/WISE experiments (Yang et al., 2009, 2010). They appear to have been generated by shoaling mode-one ISWs.

Liu et al. (1998) demonstrated, with a two-layer Gardner equation model that includes cubic nonlinearity, that ISW depressions are transformed into a train of ISWs of elevation as they propagate over sloping topography into shallower water where the upper layer is thinner than the lower layer, as did Orr and Mignerey (2003) who based their simulations on observations from the ASIAEX site. Recently Grimshaw et al. (2014) used the Ostrovsky equation to investigate the effects of rotation on the evolution of shoaling solitary waves. They too included a cubic nonlinear term. Their simulations were based on bathymetry and continuous stratifications observed in the South China Sea. They found that a significant consequence of rotation was the formation of a secondary trailing wave packet associated with nonlinear steepening of the radiated inertia gravity waves. They also conducted fully nonlinear simulations using the MITgcm. Vlasenko and Stashchuk (2007) studied three-dimensional shoaling in the Andaman Sea with a fully nonlinear nonhydrostatic numerical model using a continuous stratification. Results showed the transformation of ISWs of depression to waves of elevation as well as refraction effects.

The breaking of solitary waves travelling up slope has been addressed by several researchers. Helfrich and Melville (1986) and Helfrich (1992) considered the breaking criteria for a two-layered system. Vlasenko and Hutter (2002) performed simulations, in a continuously stratified fluid, of breaking solitary waves on slope-shelf topography and determined a parametrization for the location of wave breaking for stratifications and bathymetry based on observations in the Andaman and Sulu Seas.

The large internal solitary waves that shoal onto the Chinese Continental shelf are ~~higly~~ highly energetic features that have implications for biological productivity and sediment transport (Wang et al., 2007; Reeder et al., 2011). St. Laurent (2008) concluded that these waves drive one of the most dissipative coastal regions of the world's oceans. Thus it is important to understand their shoaling dynamics.

Observations have shown that shoaling ISWs exhibit significant structural changes (Lynch et al., 2004; Duda et al., 2004; Orr and Mignerey, 2003; Ramp et al., 2004) . Lien et al. (2012, 2014) observed waves in the vicinity of the ASIAEX experiments with recirculating cores. The generation mechanism of these waves is unclear.

In this paper we seek to better understand the evolution of shoaling waves in the South China Sea via numerical simulations. We investigate the sensitivity of the predicted shoaling behaviour to the numerical resolutions employed, finding that higher resolutions than previously used are necessary to accurately predict wave forms in shallow water. We also add to the limited understanding of the evolution of wave amplitude and currents during shoaling by determining the depths at which maximum amplitudes and currents are attained and via comparisons with adiabatic theory. The generation of mode-two waves is also clarified.

While ISWs often appear as packets we ~~have chosen to~~ consider the evolution of a single ISW for simplicity. In this first study we also ignore the important effects of background tidal currents which will modify the shoaling behaviour by introducing time varying currents and stratification. Instead we focus on exploring the sensitivity of the evolution of a single shoaling ISWs for a range of wave amplitudes to the underlying bathymetry, small changes in stratification and the effects of rotation. These simulations are based on observations from the ASIAEX experimental site (Orr and Mignerey, 2003; Duda et al., 2004; Ramp et al., 2004).

The model, bathymetries and stratifications used in this study ~~is~~ are described in Sect. 2. Results ~~of the simulations~~ are presented in Sect. 3 where sensitivity to the bathymetry, stratification, rotational effects and the potential implications of viscosity are considered. We also present results from ~~resolutions~~ resolution tests and consider the adiabaticity of the shoaling waves. Comparisons with observations from the ASIAEX and conclusions are presented in Sect. 4.

2 Modelling

2.1 Numerical model

The two-dimensional fully nonhydrostatic Internal Gravity Wave model (Lamb, 1994, 2007) is used in this study of shoaling ISWs. Flow in the along shelf y-direction is included but the flow is independent of y. The model uses the rigid-lid, traditional f-plane, Boussinesq and incompressible flow approximations. The governing equations are

$$\boldsymbol{u}_t + \boldsymbol{u}\cdot\boldsymbol{\nabla}\boldsymbol{u} - f\boldsymbol{u}\times\hat{k} = -\frac{1}{\rho_0}\boldsymbol{\nabla}p - \frac{\rho}{\rho_0}g\hat{k} + \boldsymbol{\nabla}\cdot(\nu\boldsymbol{\nabla}\boldsymbol{u}), \tag{1a}$$

$$\rho_t + \boldsymbol{u}\cdot\boldsymbol{\nabla}\rho = \boldsymbol{\nabla}\cdot(\kappa\boldsymbol{\nabla}\rho), \tag{1b}$$

$$\boldsymbol{\nabla}\cdot\boldsymbol{u} = 0, \tag{1c}$$

where z is the vertical coordinate, (x, y) are the horizontal coordinates directed across and along the topography, $\boldsymbol{u} = (u, v, w)$ is the velocity field with components in the (x, y, z) directions, $\hat{k}$ is the unit vector in the z-direction, ρ is the density, ρ_0 is the reference density, and p is the pressure. $\boldsymbol{\nabla}$ is the 3-D vector gradient operator, however all fields are independent of y. The subscript t denotes differentiation with respect to time. The gravitational acceleration is $g = 9.81\,\mathrm{m\,s^{-2}}$ and for simulations including rotational effects the Coriolis parameter is $f = 5.33\times10^{-5}\,\mathrm{s^{-1}}$ corresponding to a latitude of 21.5° N. ν and κ are a spatially varying viscosity and diffusivity, however for most of our simulations these are set to zero. The model uses flux limiting which acts to control the overturns that occur in the simulations. In the ocean strong mixing can occur. A proper account of this important problem is left for future work. Before the equations are solved, they are transformed to a terrain following coordinate system in the vertical, which leads to higher vertical resolution in shallower water. The equations are solved over a domain bounded below by the topography and a rigid lid at $z = 0$. Except for some test cases the simulations used $J = 200$ grid cells in the vertical with the height of the grid cells varying in the deep water to improve resolution across the thermocline. The model uses a variable time step to satisfy a CFL condition.

2.2 Bathymetry

Twenty five sample shelf break bathymetries in the area of ASIAEX (see red square in Fig. 1), as extracted from the Digital Bathymetry 2 min resolution (DB2) data base, are shown ~~by the grey curves~~ in Fig. 2. They contain ~~many small deviations from their average indicative of a large number~~ small scale variability indicative of the presence of small-scale~~bathymetric features which vary in the along shelf direction~~, three-dimensional bathymetric features. The solid and dotted black curves in Fig. 2a show the ~~two~~ base bathymetries used in our simulations~~, about which some variations for sensitivity studies were conducted. These bathymetries~~ . They are compared with two measured bathymetries in Fig. 2b and c and are referred to as h_0 (transect 0) and h_{15} (transect 15) bathymetries respectively. These ~~bathymetries were chosen because they~~ are representative of transects with the smallest and largest slopes~~between depths of about 500 and 2500.~~ . Bathymetric slopes are indicated in the figure. Bathymetry h_0 has a ~~uniform depth of 3000before it starts to rise gently with a slope of 0.005. The slope steepens to 0.015 at a depth of 2700, steepens again to 0.03 at a depth of 1950, decreases to 0.004 at a depth of 750and then levels off at a depth of 80. There is a~~ bump of about 200 m amplitude at ~~a depth of about~~ 2100 m ~~. The water depthat the top of the bump is about 1900. The depth then increases to about 2000after which it decreases monotonically.~~ depth. Bathymetry h_{15} ~~also starts with a gentle slope of 0.005. It steepens to 0.01 at a depth of 2700and steepens again to 0.05 for depths between 2250 and 750. This is the steepest slope for either bathymetry. The slope then decreases to 0.007 until a depth of 80is reached. Bathymetry h_{15}~~ has a 10 km long, 200 m high bump at ~~a depth of about~~ 700 m ~~separating the 0.05 and 0.007 slopes. The depthat the top of the bump is about 480~~depth. Some simulations were done with ~~a modified topography with~~ this feature removed (see Fig. 2c).

In the simulations the grid is arranged so that the shelf starts at approximately $x = 80$ km. ~~The shelf slope for bathymetry h_0 lies between -250 and 80while that for h_{15} lies between about $x = -150$ and 80.~~

2.3 Stratification and model initialization

Three ~~different~~ stratifications have been ~~considered~~ used (Fig. 3). Four stratifications are shown in the first two panels: our base stratification $\overline{\rho}_\mathrm{b}(z)$, two fits to observed stratifications measured at the ASIAEX site (Orr and Mignerey, 2003), $\overline{\rho}_1$ and $\overline{\rho}_2$, and $\overline{\rho}_\mathrm{w}$, which is the density west of Luzon Strait used in Warn-Varnas et al. (2010). Profiles $\overline{\rho}_1(z)$ and $\overline{\rho}_2(z)$ are ~~fits to two stratifications observed during the ASIAEX experiment. The observed profiles are included~~ compared with the corresponding observed profiles in Fig. 3b. These profiles were chosen because they have the thermocline at the lower and upper range of observed thermocline depths.

We initialized our simulations with internal solitary wave solutions of the governing equations (with $f = 0$) obtained by solving the Dubreil–Jacotin–Long (DJL) equation (Lamb, 2002) ~~. The DJL solver~~ which provides an initial ISW with a prescribed available potential energy (APE). ~~This procedure does not take rotational effects into account, as exact ISWs do not exist on the f-plane~~Here and throughout the APE is for waves in an infinite domain computed using the background density as the reference density (Lamb and Nguyen, 2009) . In simulations that include rotational effects ~~, appropriate to the latitude of the South China Sea, the~~ the initial waves undergo a continual adjustment which results in a continual loss of energy from the leading ISW (Helfrich, 2007; Grimshaw et al., 2014). Because of this the shoaling behaviour will depend on the initial location of the ISW. We do not consider this. The initial waves are placed in the deep water. Because of the different lengths of the shelf slopes the initial location depends on the bathymetry: for bathymetries h_0 and h_{15} the waves are started at $x = -280$ and -200 km respectively.

We have used waves with several different amplitudes based on observed amplitudes (Ramp et al., 2004). The energies and wave amplitudes for several different initial waves are provided in Table 1.

2.4 Weakly-nonlinear theory and conjugate flow amplitudes

Weakly-nonlinear theory is often used to approximate observed internal solitary waves and it provides some insight into the expected behaviour of shoaling waves. Including cubic nonlinearity and ignoring damping and rotational effects, internal solitary waves in a fluid of constant depth can be modeled with the Gardner (or extended KdV) equation

$$\eta_t + c_0\eta_x + \alpha\eta\eta_x + \alpha_1\eta^2\eta_x + \beta\eta_{xxx} = 0. \quad (2)$$

~~This equation reduces to the KdV equation when the cubic nonlinear term is ignored (i.e.~~ The KdV equation ($\alpha_1 = 0$) ~~. The KdV equation~~ predicts solitary waves of depression when $\alpha < 0$ and of elevation when $\alpha > 0$. Stratifications $\overline{\rho}_\mathrm{b}$ and $\overline{\rho}_1$ have critical points, locations where α changes sign, at depths of about 91.8 and 120.0 m respectively: in greater~~depths ISWs are waves of depression while in shallower depths , in particular on the shelf, /~~shallower depths ISWs are waves of depression/elevation. Thus for these two stratifications shoaling waves pass through a critical point on their way to the shelf which has significant implications for their evolution. Stratification $\overline{\rho}_2$, with its higher pycnocline, does not have a critical point for the chosen shelf depth of 80 m.

When $\alpha_1 < 0$ solitary wave solutions of the Gardner equation have a limiting amplitude of $-\alpha/\alpha_1$. The solitary wave solutions become flat ~~crest~~ crested as the energy in the wave increases. For $\alpha_1 > 0$ solitary waves of depression and elevation with unbounded amplitudes exist (Grimshaw et al., 2004). Using α_1 to predict the existence of solitary waves with both polarities is problematic because α_1 is not uniquely determined (Lamb and Yan, 1996). Choosing α_1 so that the second-order vertical structure function for the isopycnal displacement is zero at the depth where the leading-order eigenfunction has its maximum is a common choice (Grimshaw et al., 2002). This choice for selecting α_1 predicts that solitary waves of either polarity (i.e., elevation or depression) exist in depths greater than 235 m using our base stratification. In shallower water it predicts that only waves of one polarity exist.

Fully nonlinear ISWs generally have limiting amplitudes. As this amplitude is approached they broaden and become horizontally uniform in their centre. The flow state in the centre

of these flat-crested waves is called a conjugate flow. We computed conjugate flow solutions for depths between 50 and 400 m which provide the limiting asymptotic amplitude, propagation speeds and maximal currents for solitary waves as the wave energy goes to infinity (Lamb and Wan, 1998). The amplitudes of these solutions for the base stratification $\overline{\rho}_\mathrm{b}$ varied approximately linearly from -160 m to 20 m as the depth decreased from 400 to 60 m. Only single solutions were found with the polarity predicted by the KdV equation.

3 Results

Table 2 provides information on the simulations that have been undertaken using a deep water depth of 3000 m. ~~Information provided includes the stratification used, the initial wave energy and wave amplitude and the bathymetry used.~~

We begin by showing results for two simulations using an initial wave of amplitude 45.4 m (APE 100 MJ m^{-1}), the base stratification $\overline{\rho}_\mathrm{b}$ and the two bathymetries (Cases 2 and 3). Following this we explore sensitivity to resolution before discussing more fully the complete set of simulations.

Figure 4 shows results from Case 2. Fig. 4a shows the full continental slope and the initial wave~~which is~~ , barely visible at $x = -280$ km. After 25 h the leading wave is at $x = -64$ km where the water depth is about 650 m (Fig. 4b). A second solitary wave is visible approximately 15 km behind~~the leading wave~~. At $t = 42$ h (Fig. 4c) the leading wave, ~~approximately 1.5~~now 1.5 km in length, has reached a depth of 250 m at $x = 37$ km. Three solitary waves are now visible. By $t = 50$ h (Fig. 4d) the leading wave has significantly deformed. It is now about 3 km long ~~and spans water~~ spanning depths of 130 to 140 m. The slope of the wave front is less ~~that~~ than it was at $t = 42$ h and in the centre of the wave the ~~slope of the thermocline is greatly reduced, being almost parallel with~~ thermocline is almost parallel to the bottom (between 65.5 and 67.5 km). This is a well know feature of shoaling waves when the thermocline is close to the bottom (Vlasenko and Hutter, 2002; Orr and Mignerey, 2003; Lamb and Nguyen, 2009). The rear of the wave is much steeper and behind the leading depression the thermocline has been raised above its equilibrium position ($x = 66$

km). This we refer to as the wave pedestal. There are now three distinct waves of depression trailing the leading wave. As the leading wave continues to shoal and passes beyond the ~~critcal~~ critical point at 91 m depth (Fig. ~~4~~4e), the front part of ~~the leading depression~~ it becomes very long with a very shallow slope. On the shelf solitary waves of depression in the ambient stratification do not exist so the leading depression gradually fades away losing energy to the trailing waves. The steep back of the wave never overturns and the second solitary wave, which has now propagated into the pedestal behind the leading wave, has the form of a square wave with the centre of the wave parallel to the bottom separating a very steep front and back (Fig. ~~5e~~4e). This wave is approximately at the critical point of the background stratification but it is propagating on the wave pedestal trailing the leading wave and this is the environment it propagates in. This environment consists of a background sheared flow with ~~positive vorticity ($u_z > 0$~~negative vorticity ($u_z < 0$) and a modified stratification. By $t = 66$ h the waves are on the shelf. Breaking has commenced behind the third depression.

Figure 5 shows a close up of the leading waves and the wave breaking at $t = 66$ h. Vertical profiles of the horizontal velocity and density in the wave depressions and wave ~~pedestals~~ pedestal at the locations indicated by the vertical dashed lines are shown in Fig. 6 ~~.~~(the evolution of the shoaling waves suggests the formation of a single pedestal, which in Fig. 4e extends from the back of the leading depression at $x = 80$ km to possibly $x \approx 74$ km). In the two wave depressions (profiles D1,2 at $x = 94$ and 91 km) the horizontal velocities are similar. ~~The second pedestal (at $x = 89$) has stronger currents than the first does ($x = 92$~~In the pedestal the horizontal currents are stronger behind the second depression (profile E2) than they are ahead of it (E1). Furthermore in the ~~second pedestal~~ behind the second depression the current at the bottom has a bulge with the maximum current of about 0.5 m s^{-1} occurring about 5 m above the bottom. This is equal to the estimated propagation speed of the rear of the second ~~pedestal~~part of the pedestal ($x \approx 88.5$ km). The density profiles (Fig. 6b) show that ~~in the second pedestal~~ behind the second depression fluid in the lower 22 m is denser than the fluid ahead of the wave, a consequence of advection of dense water onto the shelf. This denser fluid can also be seen in Fig. 5 where a thin layer of this denser fluid

can be seen to extend along the bottom into the depression ahead. ~~The two pedestals have amplitudes~~ A small density overturn can be seen near the bottom of profile E2 (Fig. 6(b)). The pedestal has an amplitude of over 20 m which is well in excess of the conjugate flow amplitude of 7.7 m for the ambient stratification on the shelf. We calculated ISWs of depression for a background field given by conditions in the pedestal at $x = 92$ km by solving a version of the DJL equation that includes background currents (Stastna and Lamb, 2002; Lamb, 2003). The computed waves had a maximum amplitude of 36.6 m. At this amplitude waves are flat crested similar to the second depression centred at 90.5 km in Fig. 5. The flow in the centre of the computed solitary wave is the conjugate flow corresponding to the background conditions. Figure 6c and d compares the vertical profiles of the horizontal velocity and density field of the conjugate flow in the centre of the computed ISW with the vertical profiles from the second depression in the simulation (from $x = 91$ km). The two sets of profiles are virtually identical except near the bottom showing that the second square-shaped wave of depression is a flat-crested solitary wave riding on the background flow ~~providing~~ provided by the wave pedestal~~just ahead of it. As the velocity and density profiles in the second depression are very similar to those at the back of the leading depression (before the steep rear of the wave) at $x = 94$, the flow in the first pedestal is conjugate to the flow in the depression immediately ahead of it.~~ . The waves on the shelf have not however achieved a steady state. The amplitudes of the leading depression slowly decays (solitary waves of depression do not exist on the shelf) and as it does the amplitude of the trailing pedestal also decays as do the waves behind it.

Figure 7 shows results from a simulation using bathymetry h_{15} with the same initial wave (Case 3), now at $x = -200$ km. The results are similar to those using bathymetry h_0 but there are some differences. In both cases the shoaling wave fissions into two large solitary waves trailed by a number of smaller waves. For bathymetry h_0 the trailing waves consist largely of a couple of smaller solitary waves (at $x \approx 55$ km in Fig. 4d) whereas for the steeper bathymetry h_{15} the trailing waves are smaller and there are many more of them (e.g. Fig. 7c). The shelf slope for bathymetry h_{15} is shorter than that for bathymetry h_0 which is likely responsible for the two leading waves being closer together when bathymetry h_{15}

is used ~~. As a consequence, when the leading waves arrive on the shelf the wave pedestal between the leading and second waves of depression is much shorter for bathymetry h_{15}~~ (500 m ~~vs.~~ apart vs. 1500 m). In addition to the differences in the ~~steepness of the shelf slope bathymetry~~ bathymetric slopes h_{15} has a bump at ~~a depth of about~~ 700 m ~~, much shallower than the bump in bathymetry h_0~~depth. This bump modifies the wave field resulting in the generation of higher mode waves (Fig. 7b) as can be seen by the internal wave beam sloping up from the bump. A zoom in of the higher-mode waves at $t = 29$ h (same time shown in Fig. 7c) is shown in Fig. 8. The two dashed white boxes contain mode-two waves (the ~~second~~ left box also includes higher mode waves). Downwelling at the bottom behind the bump after the wave has passed over it can be seen ~~at $x \approx -15$ which can in some cases~~ between $x \approx -17$ and -15 km (Fig. 7b). In some cases this can result in larger vertical excursions than in the leading wave. Breaking behind the shoaling waves commences earlier for the steeper bathymetry (compare Figs. 4e and 7e). Significant wave reflection also occurs in this case due to the steeper bathymetry.

Theoretically energy is conserved as waves shoal if viscosity and diffusion is ignored, however in the simulations the total energy (kinetic plus available potential energy) changes due to numerical error. It can increase slightly in deep water due to numerical diffusion thickening the pycnocline. For case 2 the wave field at $t = 42$ h (see Figure 4c) contains 96% of the initial energy, with 90% of the initial energy contained in the wave field on the gently sloping part of the shelf slope ($x > 90$ km). The leading two solitary waves contain 50% and 16% of the initial energy. At $t = 50$ h the leading depression contains 42% of the initial energy with 7% of the initial energy now residing in the pedestal between the two leading solitary waves. At $t = 58$ h only 84% of the initial energy remains. The leading two waves of depression contain 19.9% and 10.9% of the initial wave energy while ~~the pedestal between them~~ between then the pedestal has 10.5% of the initial energy.

For Case 3 at $t = 29$ h (Figures 7(c) and 8) the energy in the full wave field is 98.8% of the original energy. The leading wave has about 36% of the original energy, vs 50% for Case 2. The second solitary wave is not cleanly separated from the trailing waves so a precise estimation of its energy is not possible however about 17% of the wave energy lies between

31 and 35 km. Approximately 15% of the wave energy is in reflected waves to the left of the bump ($x < -15$ km).

In summary, the steep slope between depths of 2250 and 750 m for bathymetry h_{15} results in significant reflection of incident wave energy. The leading solitary wave in shallow water contains less energy than for the case using bathymetry h_0 which has a gentler slope. For bathymetry h_{15} two large leading solitary waves are formed in shallow water which are trailed by a train of small amplitude mode-one and higher mode waves that are generated by the interaction of the shoaling wave with the bump. For bathymetry h_0 there are 3–4 solitary waves and the leading solitary wave has about 50% more energy that that in the other case. No trailing mode-one wave train or higher mode waves are evident. When the waves arrive on the shelf ~~large pedestals form which are~~ a large pedestal forms which is conjugate to the flow in the leading depression. These second depression waves are much larger than the largest possible solitary wave for the ambient background conditions.

3.1 Resolution

It is important to have high enough resolution to adequately resolve solitary waves as they shoal. If the resolution is too low unphysical solitary-like waves can be simulated due to a balance between nonlinearity and numerical dispersion (Hodges et al., 2006; Vitousek and Fringer, 2011). Vitousek and Fringer (2011) considered waves propagating in a 2000 m deep domain using a stratification based on observations in the South China Sea and found that resolutions coarser than about 250 m resulted in waves that were too wide.

~~We have performed a number of resolution tests.~~ In the first ~~series of tests~~set of tests, using an initial wave of amplitude 45 m and bathymetry h_{15}, the horizontal resolution was varied ($\Delta x = 250$, 100, 50, 33 and 16 m). ~~In the first set an initial wave of amplitude 45shoaled from a depth of 3000using bathymetry h_{15}.~~ The maximum time steps were 12.5, 5.0, 2.5, 2.5 and 2.5 s respectively and a uniform vertical resolution of $J = 200$ was used. For the highest resolution case the time step decreased to approximately 1.4 s by the time the wave reached the shelf. ~~Increasing~~ Doubling the time step to 5.0 s in the $\Delta x = 50$ m simulation resulted in negligible differences. After traveling over 120 km to a depth of 2500 m

the amplitudes in all five cases varied by about 2 %~~with the wave amplitude increasing as the resolution increased. By the time the waves had travelled 180to a depth of~~ . At 800 m depth, just before the bump, the solitary wave in the $\Delta x = 250$ m simulation was about 5 % smaller than that in the highest resolution case. After this stage the solutions diverged more rapidly.

Figure 9 compares the surface currents $u(x, 0, t)$ ~~at four different times~~ when the leading wave is in water depths of 600, 395, 180 and 85 m. ~~By the time the waves have reached a depth of~~ At 600 m depth (Fig. ~~10a~~9a) the leading wave has begun fissioning into several waves. The wave in the 250 m resolution case is significantly smaller than those in the other simulations while the wave in the 100 m resolution cases is almost indistinguishable from the high resolution case. At 395 m depth (Fig. ~~10b~~9b) the amplitude of the leading wave in the 250 m resolution case is grossly underestimated and has the form of a small undular bore. In contrast in the higher resolution simulations two large leading solitary waves have emerged trailed by a train of smaller waves. The amplitude of the leading wave in the 100 m resolution simulation is now about 87 % that of the highest resolution case. At ~~a depth of~~ 180 m depth (Fig. ~~10c) the amplitude of the leading wave in the 100simulation is approximately~~ 9c) this fraction has reduced to 77 %~~of that in the 33resolution case~~. The waves in the 50 m simulation are now slightly smaller than in the 33 m resolution case. In the 50 and 33 m resolution simulations the thermocline has been raised above its rest height behind the leading wave as indicated by the negative surface currents. This feature is missing at lower resolutions. At later times the 50 and 33 m resolution simulations diverge as well, becoming quite different at 85 m depth (Fig. ~~10d~~9d). The back of the leading depression becomes very steep. It is steeper in the 33 m resolution case and is resolved by 4–5 grid at both these resolutions. In the 16 m resolution case the jump is better resolved (7–8 grid points). Wave breaking has commenced behind the two leading depressions just before this time. The ~~steep rear of the waves of depression and the commencement of overturning behind them is similar to that shown in Fig. 5 for bathymetry h_0. The~~ 16 m resolution case shows much finer details and some weak overturns along the steep rear of the first square-wave depression. At this stage ~~in the evolution of the shoaling waves~~ it is

unlikely that the 16 m resolution case has converged. At depths greater than about 140 m the differences between the 50, 33 and 16 m resolution cases are not very significant.

Results from a simulation with $\Delta x = 33$ m and double the vertical resolution ($J = 400$) are indistinguishable at the scale of Fig. ~~10d~~9d.

~~Similar tests were done using~~ For a larger wave (amplitude 115 m)~~using bathymetry h_0. This wave is~~ , with approximately half the width of the 45 m wave ~~,~~ requiring higher horizontal resolutions~~. The divergence between results for different resolutions~~ , the dependence on resolution was qualitatively similar to ~~that in the above case however the divergence occurred~~ first test set with the results diverging more rapidly. ~~Indeed, after~~ After travelling 8.5 km to a depth of 2800 ~~there were already noticeable differences in wave amplitudes between the runs using $\Delta x = 250$, 100 and 33, with the~~ the wave in the 250 m resolution simulation ~~already being~~ was already over 5 % smaller than that in the 33 m simulation, ~~suggesting~~ showing that at a depth of 3000 m the resolution needs to be significantly better than 250 m to accurately simulate waves of this amplitude.

While doubling the vertical resolution did not result in any significant changes in the leading waves it did reduce noise that developed in the deep water behind the waves. When a resolution of 200 grid points was used weak (< 0.01 m s^{-1}) near surface currents (across the pycnocline at a depth of 50 m) developed over the steepest parts of the bathymetry, indicative of the pressure-gradient error that is intrinsic to sigma-coordinate models. With 400 grid points these currents were reduced by 50 %. Simulations with a resolution of 300 and 400 vertical grid points were similar and were very expensive. Because the leading waves were unaffected by increasing the vertical resolution from 200 to 400 we have for the most part used a vertically varying grid with 200 grid points in the vertical. The grid has almost uniformly spaced grid cells for depths greater than 700 m and less than 300 m in deep and shallow water with a transition region centred at 500 m depth. In deep water the resolution was between 21.1 and 21.4 m at depths greater than 700 m and decreases from 6 m in depths at 350 m depth to 5.35 m at the surface. The vertically varying grid better resolves the thermocline in deep water and improves energy conservation by reducing thickening of the pycnocline by numerical diffusion. In water with depths less than 350 m the resolution is

almost uniform, with $\mathrm{d}z = 0.4$ m on the shelf. This grid gave virtually identical results to the vertically uniform grid using 400 vertical grid points.

3.2 Adiabaticity of shoaling waves

Solitary waves are said to shoal adiabatically if they retain the form of a single solitary wave as they shoal, i.e. no fissioning or reflection occurs (Grimshaw et al., 2004; Vlasenko et al., 2005). This ~~can only~~ is an idealization that can approximately occur if the water depth changes ~~sufficiently slowly so~~ so slowly that the shoaling wave can adapt to its new depth without shedding significant energy. Adiabatically shoaling waves conserve energy to leading-order in amplitude (in the absence of rotational effects) however they are in general trailed by a long, small amplitude shelf which extends from the back of the solitary wave to the point reached by a wave, travelling at the long wave propagation speed, generated at the point when the shoaling solitary wave first encounters a depth change (Grimshaw et al., 2004). Because energy is second-order in amplitude the energy in the trailing shelf is negligible, however the mass in the shelf, being first-order in amplitude, can be significant.

~~In this section~~ Here we investigate the adiabaticity of the shoaling waves by comparing the leading wave to ISW solutions of the DJL equation having the same total energy as the initial deep water wave. Both bathymetries ~~h_0 and h_{15}~~ are used. ~~In addition we compare the shoaling behaviour of waves starting in~~ We also launch waves from different water depths using bathmetry h_0 ~~. For these comparisons the bathymetries differ only in that they level off at three different~~ leveled off at deep water depths ~~, namely of~~ 3000, 1500 and 1000 m ~~as illustrated in~~ (see Fig. 2b). The base stratification was used except where noted.

~~Internal wave~~ ISW solutions of the DJL equation were computed over a range of water depths for 11 values of the APE: 25 MJ m^{-1} and 50 to 500 MJ m^{-1} in increments of 50 MJ m^{-1}. Figure 10a shows the total wave energy E (KE plus APE) as a function of depth for these 11 values. ~~In Fig. 10b the~~ The ratio of kinetic to available potential energy ~~is shown.This ratio~~ (Fig. 10b) is always greater than one for solitary waves (Lamb and Nguyen, 2009). At 3000 m depth this ratio varies from slightly more than 1 to a maximum of 1.2 for the largest wave (amplitude 137 m) for which values are plotted. For larger waves

(not shown) this ratio continues to increase, reaching 1.3 for an APE of 800 MJ m^{-1} and 1.4 for an APE of 2 GJ m^{-1}. ~~The 800wave has an amplitude~~ These waves have amplitudes of 170 and 322 m and ~~a minimum Richardson number~~ minimum Richardson numbers of just below 0.25 ~~in the thermocline. The 2wave has an amplitude of 322, a minimum Richardson number of 0.11~~ and 0.11 respectively. For the larger wave the ratio of the maximum current to the propagation speed is $\max(u)/c = 0.98$. Waves with $\max(u)/c > 1$ have cores of recirculating fluid.

As the water depth decreases from 3000 m with the APE fixed the total wave energy increases due to the increasing KE/APE ratio, reaching a peak value at depths between about 400 and 1200 m for small and large waves (KE/APE ≈ 1.16 and 1.3 respectively, Fig. 10b). As the depth decreases further the total energy rapidly decreases to twice the APE. This near equipartition of energy suggests waves of smaller amplitude. This is indeed borne out in Fig. 11 which shows the wave amplitude (maximum isopycnal displacement), maximum surface current and maximum bottom current (negative for rightward propagating waves of depression) as a function of depth for constant total energies E of 50 MJ m^{-1} and 100 to 1000 MJ m^{-1} in increments of 100 MJ m^{-1}. These values were obtained by interpolating results from the DJL solutions, for which the APE is prescribed, and will be referred to as the adiabatic curves: these are the curves a shoaling wave would follow if the wave preserved its total energy and maintained the form of a solitary wave for its depth. As the water depth decreases from 3000 m the wave amplitude increases significantly, reaching a maximum value in depths between 300 and 600 m. The largest wave (total energy of 1 GJ m^{-1}) increases in amplitude by a factor of 1.4 from 129 to 183 m. For smaller waves the amplitudes increase by larger factors as the depth decreases (e.g. 3.5, 2.9 and 2.3 for the three smallest waves). ~~Once shallow water is reached the amplitudes decrease rapidly and all waves have an amplitude~~ Amplitudes thereafter decrease rapidly to close to 60 m in water of 200 m depth. This is an indication of the conjugate flow limit being attained: the waves all have the same maximum amplitude and as the wave energy increases the waves get longer with negligible increases in amplitude.

The adiabatic curves are similar for the other two stratifications. Table 3 gives the initial and maximum amplitudes and the depth at which the maximum amplitude occurs for ISW solutions of the DJL equation for waves of fixed total energy ~~. The maximum amplitudes and depths are based on values computed at depth intervals of 50. Values~~ for all three stratifications~~are provided~~. The increase in amplitude of the waves is similar for stratifications $\overline{\rho}_\mathrm{b}$ and $\overline{\rho}_1$ while waves using stratification $\overline{\rho}_2$ show a larger amplitude increase, particularly for small waves.

A similar pattern is seen for the maximum surface currents except that the maximum currents occur in greater depths than do the maximum wave amplitudes and the range of depths at which near-maximum currents occur is much wider than those for near-maximum amplitudes. The bottom currents reach their maximum values in much shallower water and the increase over their deep water values is much larger than the increases in wave amplitude and surface currents.

Figure 11 also shows the maximum wave amplitude, maximum surface current and minimum currents at the bottom from several simulations. For these simulations ~~the Coriolis parameter was set to zero~~ $f = 0$, as the adiabatic curves are only appropriate in the absence of rotation. Five simulations were done using bathymetry h_0. Four of these used a horizontal resolution of about 33 m with 200 uniformly spaced grid points in the vertical (blue curves). These waves had APEs of 50, 100, 250 and 400 MJ m^{-1}. The fifth case (black dash-dot), also with an APE of 400 MJ m^{-1}, used double the vertical resolution. It largely overlies the corresponding lower resolution case. Results from simulations using bathymetry h_{15} are also shown (red curves). The initial APEs for waves launched from 3000 m depth were 100, 150, 250 and 400 MJ m^{-1}. The wave started at a depth of 1500 m had an initial APE of 375 MJ m^{-1}, chosen so the total wave energy is similar to that of the wave with an APE of 400 MJ m^{-1} started at 3000 m depth. Waves launched from 1000 m depth had APEs of 50, 60, 70 and 100 MJ m^{-1}.

Figure 11a and b show that the wave amplitudes and maximum surface currents tend to increase more slowly than the adiabatic curves in deep water and follow them more closely

in shallow water. The depths at which they begin to follow the adiabatic curves more closely depends on the bathymetry and wave amplitude.

Consider the results obtained using bathymetry h_0 (blue curves) which has a bump at a depth of about 2000 m. When the wave launched at a depth of 3000 m with an APE of 400 MJ m^{-1} (initial amplitude 115 m, $E = 847$ MJ m^{-1}) first reaches the crest of the bump (depth 1900 m) its amplitude is equal to that of a solitary wave with E equal to 750 MJ m^{-1} while the maximum surface current corresponds to that for a wave with a total energy of 670 MJ m^{-1}. By the time the wave has passed over the bump and shoaled to a depth of 1900 m for the second time the wave amplitude and, to a much greater degree, the maximum surface current, have increased to the values corresponding to an ISW with energies closer to that of the original wave. The increase in the maximum surface current is particularly striking. This is an indication the wave is not shoaling adiabatically, i.e. that is it has not fully adjusted to the change in water depth. Results for this wave track an adiabatic curve for depths less than about 1600 m.

Results for the other wave amplitudes are similar. In contrast to the adiabatic curves, the two smallest waves launched from a depth of 3000 m show little increase in the wave amplitude and maximum surface current until they have reached depths of about 750 m, where the bottom slope decreases from 0.03 to 0.004. At this point the amplitude and maximum surface current of the wave with an initial APE of 100 MJ m^{-1} ($E = 204$ MJ m^{-1}) is well below those for the DJL waves with an initial APE of 50 MJ m^{-1}. After this the amplitudes and surface currents rise rapidly and fall tracking the adiabatic curves in depths less than about 700 m. This suggests significantly non-adiabatic shoaling over the steep slope and nearly adiabatic shoaling over the gentle slope between depths of 750 and 80 m. Similar behaviour is observed for the waves launched from a depth of 1000 m.

Results obtained using bathymetry h_{15} show a similar pattern. Because this bathymetry is much steeper than h_0 for depths between 500 and 2300 m, the results with this bathymetry (red curves) do not follow the adiabatic curves until the waves reach much shallower depths of between 500 and 600 m. The effects of the bump at a depth of 600 m are clearly visible. The large loops in the wave amplitudes, particularly evident in the smaller waves, are a con-

sequence of the largest ~~vertically~~ vertical displacements occurring behind the bump after the solitary wave passes over it, rather than in the solitary wave itself, for a short period of time.

In water shallower than about 400 m the large shoaling waves have amplitudes that exceed the conjugate flow limit by as much at 50%: at 350 and 200 m depths the largest shoaling waves have amplitudes of 142 and 95 m while the corresponding conjugate flow amplitudes are 137 and 61 m. Surface currents do not exceed the conjugate flow limits until depths of 250 m are reached.

Figure 11c shows the evolution of the strongest bottom currents. ~~The most striking feature is that the bottom currents~~ They greatly exceed those for the DJL solutions in water shallower than about 300 m for the large waves and about 200 m for the smaller waves. This is a consequence of the fluid below the thermocline being squeezed out from beneath the waves as the waves shoal which, in shallow water, results in enhanced bottom currents. This has important implications for the occurrence of instabilities, mixing and sediment resuspension beneath the shoaling wave. Also noteworthy is that for the large waves the bottom current increases relative to the adiabatic curves as the waves shoal to about 500 m depth. For the smaller waves they decrease as do the amplitudes and surface currents. For large waves in shallow water the bottom currents greatly exceed the surface currents.

In summary, the amplitudes and maximum surface and bottom currents of the shoaling waves qualitatively follow the behaviour expected of a wave that is shoaling adiabatically however there are some significant differences, a consequence of the timescale of depth changes experienced by the shoaling wave being shorter than the time required for the waves to adjust to their new depth. The amplitude and surface currents increase more slowly in deep water, particularly over the steep slope between depths of 2250 and 750 m for bathymetry h_{15}. Part of the difference can be ascribed to the waves having not fully adjusted to the changing depth rather than to fissioning as illustrated by the behaviour as the waves pass over the bump at a depth of 2000 m for bathymetry h_0. For depths between about 1000 and 400 m the properties of the shoaling waves track the adiabatic curves very

well. In shallower water the waves can have amplitudes more than 50% larger than any exact solitary wave at that depth while currents at the bottom can be twice as large.

3.3 Sensitivity to initial water depth

For reasons of numerical efficiency it is tempting to truncate the bathymetry and start waves from depths of, say, 1000 m. Here we briefly explore the implications of doing so.

Figure 12 compares the horizontal surface current and ~~$\sigma_t = 0.0232$~~$\sigma_\theta \equiv \rho - 1000 = 23.2$ kg m^{-3} isopycnal at different times for ~~shoaling waves~~ cases with initial APEs of 60 and 100 MJ m^{-1} launched from depths of 1000 and 3000 m respectively using bathymetry h_0. The latter case is Case 2 illustrated in Fig. 4. The chosen isopycnal is at the depth of maximum buoyancy frequency in the undisturbed stratification. It is not the isopycnal which undergoes maximum vertical displacement in the wave ~~. The latter isopycnal~~ which varies with wave amplitude and ~~varies~~ as the wave shoals.

These two waves are chosen because in shallow water the leading waves have nearly identical amplitude. At a depth of 750 m (Fig. 12a,b), where the shelf slope decreases from 0.03 to 0.004, the waves are about 15 km and 150 km beyond the bottom of their shelf slopes. Both waves are asymmetric, with the wave launched from deeper water being much more asymmetric. By the time the wave has reached a depth of 560 m the wave launched from the deeper/shallower water has fissioned into three/two solitary waves (not shown). At a depth of 250 m (Fig. 12c,d) the multiple solitary waves produced via fissioning are well separated. The third wave in Case 2 has a similar amplitude and location to that of the second wave for the case started at 1000 m depth. The pedestal behind the leading wave is starting to form. By the time the waves have reached depths of about 120 m (Fig. 12e,f) the third wave in the deep water case has now split into two waves.

As the waves pass the critical point and reach their final depth of 80 m (Fig. 12g,h) the leading wave continues to broaden and the currents decay in amplitude. The second wave in the deep water case advances into the wave shelf trailing the leading wave (the region of negative surface current) with the result that the wave forms behind the leading depression are quite different for the two cases.

Truncating the deep water depth to 1000 m significantly modifies the fissioning processes resulting in fewer waves, reducing the relative amplitude of the second solitary wave and increasing the distance between the two leading waves.

3.4 Effects of small scale bumps

The deep bump on bathymetry h_0 does not significantly affect the evolution of the shoaling waves. The much shallower bump on bathymetry h_{15} has a significant impact. Figure 13 compares the wave fields at $t = 29$ and 34 h for simulations with and without the bump for an initial wave amplitude of 59 m (APE 150 MJ m^{-1}, Case 4). ~~For the bathymetry with the~~ With the bump the leading three waves at $t = 29$ h are at $x = 41.0$, 35.9 and 31.8 km. With the bump removed the waves are slightly ahead, at $x = 42.8$, 37.3 and 33.7 km which we attribute to the reduction in propagation speed as the wave passes over the bump. The bump also results in a reduction in wave amplitude, with the leading three waves containing 60% and 71% of the initial wave energy for cases Cases 4 and 4nb.

The most striking difference between the two simulations is the wave field behind the leading three waves. For Case 4 a small amplitude mode-one wave train trails the leading three waves. Following are higher mode waves, e.g. at time $t = 29$ (Fig. 13a), a concave mode-two wave is centred at ~~about~~ $x = 16$ km and a convex mode-two wave (and higher mode waves) lies between $x = 0$ and 6 km with higher mode waves further behind and a wave beam sloping up to the right above the bump. At the later times mode-two waves in both simulations are clearly apparent~~but~~, however with the bump there is a mode-two concave wave ($x = 30$ km) followed by a train of mode-two waves (between $x = 16$ and 20 km) whereas without the bump there is a single convex mode-two wave at $x = 20$ km. The bump also results in reflected waves containing about 6% of the initial wave energy (less than the 15% reflected for Case 3 discussed in section 3.1). ~~Without the bump~~ In Case 4nb energy in the reflected waves is insignificant.

3.5 Sensitivity to initial wave amplitude

Figure 14 compares the shoaling behaviour for three initial waves (amplitudes 45, 83 and 115 m) using the base stratification $\overline{\rho}_\mathrm{b}$ and bathymetry h_{15} (Cases 3, 6, and 7). Times for comparison are chosen so that the leading waves are in approximately the same location. For the smallest initial wave there are two large solitary waves at $t = 35$ h (Fig. 14b) whereas for the two larger waves there are three. The intermediate wave has a number of smaller solitary waves trailing the leading large waves that are absent in the two cases with smaller and larger initial waves. At the early times shown (panels a, c, e) the leading wave contains 36%, 53% and 75% of the initial wave energy showing a striking increase with the initial wave amplitude. The higher mode waves are similar for these three cases (not shown).

3.6 Effects of rotation

The effects of rotation on the evolution of the internal tide and on ISWs has been considered by many authors (e.g. Helfrich, 2007; Helfrich and Grimshaw, 2008; Grimshaw et al., 2014). Rotation makes long ~~wave~~ waves dispersive and as a consequence ISWs radiate long inertia-gravity (Poincaré) waves behind them and gradually decrease in amplitude. In some regions of parameter space the long radiated waves steepen and form new ISW packets (Helfrich, 2007). This process takes place on the inertial time period which in the South China Sea is about 32 h. This is comparable to the shoaling times in our simulations so it is clear that rotational effects will significantly affect waves launched from the deep water by the time they reach the shelf.

The effects of rotation on the shoaling of ISWs was investigated using bathymetry h_{15} with the initial waves at $x = -200$ km. Starting the waves further from the shelf would increase the effects of rotation by reducing the amplitude of the wave at the bottom of the shelf slope and by introducing a long inertia-gravity wave behind the leading solitary wave. As a proxy for the first effect we can simply consider waves with different initial amplitudes.

Figure 15 compares the ~~$\sigma_t = 0.0232$~~$\sigma_\theta = 23.2$ kg m^{-3} isopycnals at different times for Cases 3(r) and 5(r)~~, which use two different initial wave amplitudes, for $f = 0$ and~~

$f = 5.35 \times 10^{-5}$. Figures 15a–c show results for an initial wave amplitude of 45.4 m (Case 3 and 3r). At $t = 23$ h (Fig. 15a) the leading wave in the non-rotational case is just past the bump at 610 m depth. The isopycnal undergoes a maximum downward displacement of about 46 m. At this location the $\sigma_t = 0.0232$ $\sigma_\theta = 23.2$ kg m^{-3} isopycnal is not the isopycnal undergoing maximum displacement (the amplitude of the leading wave is about 53 m). In the rotational case the leading wave trails by almost 2 km and the isopycnal undergoes a maximum downward displacement of 26 m, almost half that in the non-rotating case. At this point the wave has been travelling for about three quarters of an inertial period and has propagated 200 km. It is no surprise then, that in the rotational case the leading wave has been significantly modified. The long small amplitude wave of elevation between $x = -25$ and -12 km is slightly larger in the rotational case. The currents in the rotational case are much larger than those in the non-rotating case (not shown). After 35 h (Fig. 15b) the leading waves have reached a depth of about 200 m. At this depth the wave amplitude is strongly controlled by the water depth and the waves in the non-rotating and rotating cases have similar amplitudes, with the wave in the non-rotating case being much wider. In the non-rotating case three ISWs are present. There are only two in the rotating case. The wave of elevation between $x = 30$ and 50 km is larger in the rotating case (surface currents are twice as strong) and in the rotating case it subsequently steepens and forms a secondary packet of short waves (between $x = 67$ to 70 km at $t = 45$ h, Fig. 15c) which is not present in the non-rotating case. Such wave packets were reported by Grimshaw et al. (2014).

Figure 15d–e show results for larger initial waves (71.6 m, Cases 5 and 5r) and similar trends are observed. The secondary wave packet does not form in this case because its formation is disrupted by wave breaking behind the leading mode-one solitary waves. Starting the initial wave further away would give more time for the secondary wave packets to form hence potentially making them more prominent.

Fig. 16 shows the amplitude of the leading wave as a function of x as the waves shoal. Results for five pairs of simulations (with and without rotation) using different initial wave amplitudes are shown (cases 3–7). In the absence of rotational effects the When $f = 0$ the waves slowly increase in amplitude until the bump ($x = -20$ km) is reached. At this stage

the wave fissions and the amplitudes of the three smallest waves momentarily decrease. All waves then rapidly increase in amplitude. The largest wave reaches its peak amplitude just before the crest of the bump is reached, then maintains its amplitude before starting to decrease in amplitude rapidly at $x = 40$ km (420 m depth). The other waves reach their maximum amplitude between $x = 40$ and 50 km (depths of 400–300 m) before rapidly decreasing until the shelf is reached at $x = 80$ km with smaller waves reaching their maximum amplitude in shallower water.

When rotational effects are included the wave amplitude immediately starts to decrease, approximately linearly with x. After passing over the bump at $x = -20$ km the effects of rotation on the leading wave no longer seem to be prominent, with the amplitude varying similarly to those in the non-rotating cases.

3.7 Sensitivity to stratification

~~The stratification at the ASIAEX site varied over the course of the field program. Here we~~ We next consider the sensitivity of ~~the shoaling behaviour to various in stratification~~ wave shoaling to variations in stratification similar to those observed over the course of the ASIAEX field program. The major difference in our stratifications is the depth of the thermocline which also acts as a proxy for the raising and lowering of the thermocline in reponse to ~~the internal tides in the region~~ locally generated internal tides and other subtidal currents which are not included in our simulations. Ramp et al. (2004) report on the influence of the internal tides on the wave forms in shallow water.

Figure 17 compares waves fields for the three stratifications ($\overline{\rho}_b$, $\overline{\rho}_1$, and $\overline{\rho}_2$, see Fig. 3) using bathymetry h_{15}, $f = 0$ and an initial wave APE of 100 MJ m^{-1}. These plots show the leading waves after they have reached the shelf along with trailing mode-one and higher mode waves. For stratification $\overline{\rho}_b$ (Fig. 17a) the shoaling solitary waves encounter a critical point and solitary waves are waves of elevation on the shelf. In this case the leading depression is very broad and decays with time. The pedestals will ultimately yield solitary waves of elevation. For stratification $\overline{\rho}_1$ (Fig. 17b) the pycnocline is lower in the water column and the critical point is reached at greater depth. In this case breaking has resulted in

almost complete destruction of the pedestals. For stratification $\overline{\rho}_2$ (Fig. 17b) the pycnocline is above the mid-depth on the shelf and solitary waves of depression persist. In this case it can be seen that the leading depression has a steep front (at approximately $x = 86$ km), in constrast to the other cases. Ultimately a broad square-shaped solitary wave of depression will form. Ramp et al. (2004) observed waves of depression at 120 m depth during times when the internal tide had raised the thermocline above the mid-depth (their Figure 6, 18:00 GMT May 13 to 06:00 GMT May 14), some of which have the appearance of broad waves of depression (e.g., between 23:00 and 02:00).

In Case 3 ($\overline{\rho}_b$, Fig. 17a) a packet of short small amplitude mode-one waves is present between about 60 and 80 km that is absent from the other two cases, while in Case 12 ($\overline{\rho}_2$, Fig. 17c) there is a short packet of mode-one solitary waves between 60 and 62 km that is not present for the other two stratifications. The mode-two wave field also shows some differences. For Case 9 ($\overline{\rho}_1$, Fig. 17b) a long convex mode-two wave is present between $x = 44$ and 50 km. For the other stratifications mode-two wave trains have been generated along with concave mode-two waves at $x = 53$ and 50 for Cases 3 and 12 respectively.

Rotation modifies the wave fields (Fig. 18). The leading mode-one waves on the shelf are similar but smaller in amplitude. The mode-two waves are also similar to those in the corresponding non-rotating cases. The striking differences between the rotating and non-rotating cases are the large mode-one wave packets in the rotational cases (at $x = 67$–70, 69–73 and 60–64 km in Cases 3r, 9r, 12r respectively) that have been generated by the nonlinear evolution of the inertia-gravity waves that form behind the shoaling solitary wave ~~. This phenomena was reported by Grimshaw et al. (2014) .~~ (Grimshaw et al., 2014) . The mode-one wave packet was also present in Case 12 but is much larger in the rotating case.

3.8 Effects of viscosity and boundary layer separation

In the real world shoaling waves are subject to a no-slip bottom boundary conditions and the effects of boundary layer instabilities as well as diffusion and dissipation related to other physical processes, in particular tidal currents. ~~In order to point out~~ To illustrate the potential implications of these processes some simulations were done with vertical eddy

viscosity/diffusivity ~~of the form~~

$$\nu = \kappa = K f(z) = K \,\mathrm{sech}\left(\frac{z - h(x)}{h_s}\right) \tag{3}$$

using a scale height $h_s = 10.0\,\mathrm{m}$. The dimensionless function $f(z)$ is shown in the left panel in Fig. 19. The diffusivity/viscosity has a maximum value of K at the bottom and decreases by factors of 10 and 100 approximately 30 and 53 m above the bottom. This form of the viscosity/diffusivity coupled with a no-slip bottom boundary condition results in flow separation and vortex shedding at the back of the shoaling ISWs (Lamb and Nguyen, 2009; Boegman and Ivey, 2009; Lamb, 2014). The functional form of the eddy viscosity/diffusivity is ad-hoc. We take the point of view that physically what is important is a mechanism to create boundary layer separation and vortex shedding off the boundary and we do this in a simple way while confining the viscosity/diffusivity to a region close to the bottom boundary. ~~We consider~~ Use of three different values of K ~~to illustrate of~~ illustrate the sensitivity of the results to its value.

Figure 19 compares results from an inviscid simulation (Fig. 19a,b) with results from simulations with $K = 10^{-5}$, 10^{-4} and $10^{-3}\,\mathrm{m^2\,s^{-1}}$. The latter is possibly unrealistically large. At the stage illustrated, the four solutions have just become noticeably different in form (when the lead waves are at $x = 59\,\mathrm{km}$ all four results are very similar~~with amplitudes decreasing with K~~). For $K = 10^{-5}\,\mathrm{m^2\,s^{-1}}$ (Fig. 19c,d) the most noticeable difference is the enhancement of the positive near bottom currents beneath the first part of the pedestal ($x = 68.5\,\mathrm{km}$). This is consistent with flow separation and the formation of a vortex behind the leading depression as has been observed in the laboratory and in lab-scale numerical simulations. This positive current behind the leading depression is strengthened as K increases. For $K = 10^{-4}\,\mathrm{m^2\,s^{-1}}$ (Fig. 19e,f) the waves are starting to deform. For the largest value of K the leading depression is significantly reduced in length and the trailing waves are smaller and show small scale features. In shallower water the differences between the four cases grow.

These results and results from other simulations not shown suggest that viscous effects are not significant until the waves reach depths less than about 200 m however in deeper

water the vertical resolution is reduced so these results are merely suggestive. In deep water the near bottom currents are much weaker which would reduce the ~~affects~~ effects of the bottom boundary layer beneath the shoaling waves. Observations of sand dunes in the northern South China Sea reported by Reeder et al. (2011) at depths between 160 and 600, m suggest that bottom boundary layer processes could be important at depths greater than 200 m. Our simulations suggest that the presence of a turbulent bottom boundary layer beneath the waves could significantly affect shoaling solitary waves in water depths less than 200 m however these results are quite sensitive to the eddy viscosity. A more detailed investigation is needed.

4 Discussion and conclusions

Using a two-dimensional non-hydrostatic primitive equation model we have investigated aspects of the shoaling behaviour of internal solitary waves in the northeastern South China Sea using bathymetry and stratifications based on observations made in the vicinity of the ~~Asian Seas International Acoustic Experiment~~ ASIAEX site (Orr and Mignerey, 2003; Duda et al., 2004; Ramp et al., 2004). Sensitivity to the stratification, the bathymetry and the effects of rotation were considered. The majority of the simulations were done without explicit viscosity. A few runs were done to explore the potential implications of a no-slip bottom boundary condition and the presence of a turbulent bottom boundary layer. Consideration of the effects of concurrent barotropic tides on shoaling ISWs are left for future work.

While waves with amplitudes close to 200 m have been observed in the deep part of the South China Sea (Klymak et al., 2006; Lien et al., 2012, 2014), we considered initial waves with amplitudes between 30 and 115 m in water 3000 m deep which are more typical (Li and Farmer, 2011). The adiabaticity of the shoaling was considered by tracking the wave amplitude and maximum wave induced currents as a function of water depth as the waves shoaled and comparing them with values along the adiabatic curves (~~internal solitary waves~~ ISWs with constant energy). ~~We found some significant deviations from the adiabatic curves, with the amplitudes and~~ The amplitudes and surface currents during shoaling ~~being~~

~~significant~~ are significantly less than those for an adiabatically shoaling wave in deep water but can be much larger in very shallow water. Thus the bathymetry in the vicinity of the ASIAEX site is steep enough to result in significant deviations of the shoaling wave from ~~a solitary wave~~ an ISW solution of the DJL equation with the same initial energy. Some energy is lost by fissioning of the initial wave into multiple waves ~~. An example is that of~~ (e.g., Case 2~~shown in~~ , Figs. 4 and 5~~. This case~~). Case 2 also illustrates the common occurrence of wave breaking in waves behind the leading depression (in this case at the back of the third wave of depression). Because of the very steep rear of the shoaling waves high horizontal resolutions were necessary. For most of our simulations we used a horizontal resolution of 33 m. The trailing waves did depend on the initial water depths. Comparisons of the shoaling behaviour of solitary waves with different deep water depths were done in which we tuned the amplitude of the wave starting in water of 1000 and 1500 m depths so that in water depths of less than 1000 m the leading waves had the same amplitude. The wave starting in the deeper water had larger trailing waves, an indication of the non-adiabatic nature of the shoaling even in deep water. Thus, in order to make detailed comparisons with observations it will be important to start at an appropriate deep water depth.

The bumps on the shelf slope topography influenced the shoaling behaviour, particularly the shallower bump on bathymetry h_{15} which is about 200 m high in water 700 m deep. As the shoaling wave passes over this bump higher mode waves are formed. As the bumps in the bathymetric transects are slices through three-dimensional features this implies that three-dimensionality of the bathymetry is likely an important factor in some locations, particularly for the secondary waves that form during shoaling, though the effects of bumps may be mitigated in three-dimensions because the flow could go around them.

In the absence of rotation, shoaling waves grow slightly in amplitude until they reach water depths of 800–1000 m after which they rapidly grow, reaching their maximum amplitude at depths between 250 and 600 m for initial amplitudes of 45 and 115 m respectively. They then decrease rapidly in amplitude but large waves can be 50 % larger than the conjugate flow amplitude limit in water of 200 m depth. Rotation results in a continuous decrease in wave amplitude as waves shoal from 3000 m depth to 1000 m depth due to the continual

radiation of inertia-gravity waves, but thereafter the waves undergo the same rapid rise and fall of their amplitude as they shoal into shallower water.

Ramp et al. (2004) presented time-depth temperature contour plots of internal waves at depths of 350, 200 and 120 m spanning an 11 day period. At 350 m depth they reported wave amplitudes (based on the 24° isotherm, hence amplitudes potentially underestimated) ranging between 29 and 142 m which matches well with the range of amplitudes in our simulations. Many features of the observed waves are similar to those seen in our simulations although there is naturally a great deal of variability in the observed waves. At 350 m depth both the observed and simulated waves were fairly symmetric. At 200 m depth many of the observed waves and all of the simulated waves were quite asymmetric (see also Fig. 4 in Orr and Mignerey, 2003 which shows acoustic images of an asymmetric wave close to this depth). As an example of a wave which is similar to one ~~of~~ in our simulations consider the a wave observed at 08:00 GMT on 7 May (see Fig. 4 and Table III in Ramp et al., 2004). At 350 m depth it had an amplitude of 110 m and appears reasonably symmetric (note, however the difference in stratifications ahead and behind the wave suggesting that the observed wave is propagating at the front of a long depression). Four hours later it arrived at the 200 m depth mooring at which point it is quite asymmetric with the back of the wave being much steeper than the front of the wave. In our Case 6, which had an initial amplitude of 83.1 m, the leading wave had an amplitude of 117 m at 350 m depth at which point it was about 1.5 km in width and had a propagation speed of 1.6 m s^{-1}. Ramp et al. (2004) report a propagation speed of 1.33 m s^{-1} and a width of 760 m (twice their reported half-width) for their observed wave. At 200 m depth the wave in our simulation had widened to 2 km and the propagation speed had decreased to 1.0 m s^{-1}. The wave was also asymmetric as is the observed wave~~(Ramp et al., 2004)~~. Using a propagation speed of 1 m s^{-1} the observed wave also has a width of about 2 km. By the time the observed waves have reached a depth of 120 m they have broken up into many smaller waves including waves of elevation superimposed on broad depressions. Our simulations with viscosity suggest that by this depth the waves may have been strongly modified by bottom boundary layer processes.

Many of the observations from the ASIAEX program show waves that are broad, with a gently sloping front and steep back, in water of 120 and 85 m depth (Ramp et al., 2004; Lynch et al., 2004; Duda et al., 2004). These are , often trailed by a small number of narrow waves of elevation and square shaped depressions as in our simulations. Figure 3 in Duda et al. (2004) shows the presence of waves of elevation in which the thermocline is raised above its rest height in a water depth of 85 m similar to the pedestals generated in out our simulations. Ramp et al. (2004) show several examples (e.g., 14:00-16:00 GMT on May 7, 15:00:16:00 GMT on May 9, their Figure 6) in which near bottom water is raised well into the water column in waves of elevation trailing a broad wave of depression in water of 120 m depth.

In our simulations we start with a single solitary wave in deep water. The shoaling wave fissions into several waves, with at least two well separated solitary waves having been formed by depths of 600–700 m for both bathymetries, with the waves separating at greater depth for bathymetry h_0 which has the more gentle slope. For the steeper bathymetry the waves have reached shallower water before completely separating. In contrast, Lynch et al. (2004) and Ramp et al. (2004) report that large solitary waves at a depth of 350 m have split into two by the time they reach a depth of 200 m.

During the ASIAEX program only one mode-two wave was observed (Lynch et al., 2004). In a pilot program Yang et al. (2004) observed a single mode-two wave in water 426 m deep. Yang et al. (2009, 2010) analyzed mooring data obtained during the VANS/WISE program which was conducted in 2005 and 2006 in the vicinity of the ASIAEX field program. Data from a mooring deployed along the 350 m isobath was analyzed showed the occurence of many mode-two waves. They appeared in two forms: convex mode-two waves in which there is a bulge in the thermocline with isotherms raised/lowered in the upper/lower part of the water column, and concave mode-two waves with isotherms displaced in the opposite directions. Convex mode-two waves were by far the most common. The mode-two waves trailed mode-one waves suggesting that they were generated via the adjustment of shoaling mode-one waves (Yang et al., 2009). Stratification and seasonal variations played a role in

generation of mode-two ISWs with mode-two waves more common in winter (Yang et al., 2009).

Our simulations also showed the formation of both convex and concave mode-two waves which evolved from the shoaling mode-one wave, as observed by Yang et al. (2009, 2010). In the simulations they were present at the depths of the observed waves. Their presence and amplitude were sensitive to the stratification and to rotational effects. The shallow bump on bathymetry h_{15} led to the generation of a mode-two wave train and made the mode-two ISWs more prominent (see Fig. 13). The generation mechanisms of mode-two ISWs, their frequency of occurrence, and locations on the continental shelf require further study.

An important process not considered in this study is the influence of barotropic tides and background currents on the shoaling of internal solitary waves. The advection of the shoaling wave by on-shelf and off-shelf tidal currents will decrease and increase the time the waves have to adjust – effectively increasing and decreasing the slope. In addition the on- and off-shelf motion will modify the stratification experienced by the waves and will generate other waves for the shoaling wave to interact with. Our simulations with near-bottom eddy viscosity suggest that the shoaling waves may be significantly modified by viscous effects in water shallower than 200 m, though our simulations are not well resolved in deep water so this remains an open question. Clearly much remains for us to learn about the evolution of shoaling ISWs.

Acknowledgements. This work is supported by the Office of Naval Research under PE 62435 (A. Warn-Varnas) and grants from the Natural Sciences and Engineering Research Council of Canada (NSERC) and the Canadian Foundation for Innovation (K. Lamb). The facilities of the Shared Hierarchical Academic Research Computing Network (SHARCNET:www.sharcnet.ca) and Compute/Calcul Canada were used for some of this work.

References

Alford, M. H., Lien, R. C., Simmons, H., Klymak, J., Ramp, S., Yang, Y. J., Tang, D., and M.-H. Chang.: Speed and evolution of nonlinear internal waves transiting the South China Sea, J. Phys. Oceanogr., 40, 1338–1355, doi:10.1175/2010JPO4388.1, 2010.

Apel, J. R., Holbrook, J. R., Liu, A. K., and Tsai, J. J.: The Sulu Sea internal soliton experiment, J. Phys. Oceanogr., 15, 1625–1641, 1985.

Boegman, L. and Ivey, G. N.: Flow separation and resuspension beneath shoaling nonlinear internal waves, J. Geophys. Res., 114, c02018, doi:10.1029/2007JC004411, 2009.

Buijsman, M. C., Kanarska, Y., and McWilliams, J. C.: On the generation and evolution of nonlinear internal waves in the South China Sea, J. Geophys. Res., 115, C10057, doi:10.1029/2009JC006004, 2010.

Duda, T. F., Lynch, J. F., Irish, J. D., Beardsley, R. C., Ramp, S. R., Chiu, C.-S., Tang, T. Y., and Y.-J.Yang: Internal tide and nonlinear wave behavior at the continental slope in the northern South China Sea, IEEE J. Oceanic Eng., 29, 1105–1130, doi:10.1109/JOE.2004.836998, 2004.

Farmer, D., Li, Q., and Park, J.-H.: Internal wave observations in the South China Sea: the role of rotation and non-linearity, Atmos. Ocean., 47, 267–280, doi:10.3137/OC313.2009, 2009.

Grimshaw, R., Pelinovsky, E., and Poloukhina, O.: Higher-order Korteweg-de Vries models for internal solitary waves in a stratified shear flow with a free surface, Nonlin. Processes Geophys., 9, 221–235, doi:10.5194/npg-9-221-2002, 2002.

Grimshaw, R., Pelinovsky, E. N., Talipova, T. G., and Kurkin, A.: Simulations of the transformation of internal solitary waves on oceanic shelves, J. Phys. Oceanogr., 34, 2774–2791, 2004.

Grimshaw, R., Guo, C., Helfrich, K., and Vlasenko, V.: Combined effect of rotation and topography on shoaling oceanic internal solitary waves, J. Phys. Oceanogr., 44, 1116–1132, doi:10.1175/JPO-D-13-1094.1, 2014.

Guo, C. and Chen, X.: A review of internal solitary wave dynamics in the northern South China Sea, Prog. Oceanogr., 121, 7–23, doi:10.1016/j.pocean.2013.04.002, 2014.

Helfrich, K. R.: Internal solitary wave breaking and run-up on a Uniform Slope, J. Fluid Mech., 243, 133–154, 1992.

Helfrich, K. R.: Decay and return of internal solitary waves with rotation, Phys. Fluids, 19, 026601, doi:10.1063/1.2472509, 2007.

Helfrich, K. R. and Grimshaw, R. H. J.: Nonlinear Disintegration of the Internal Tide, J. Phys. Oceanogr., 38, 686–701, doi:10.1175/2007JPO3826.1, 2008.

Helfrich, K. R. and Melville, W. K.: On long nonlinear internal waves over slope-shelf topography, J. Fluid Mech., 167, 285–308, 1986.

Hodges, B., Laval, B., and Wadzuk, B.: Numerical error assessment and a temporal horizon for internal waves in a hydrostatic model, Ocean Model., 13, 44–64, doi:10.1016/j.ocemod.2005.09.005, 2006.

Hsu, M.-K. and Liu, A. K.: Nonlinear internal waves in the South China Sea, Can. J. Remote Sens., 26, 72–81, 2000.

Klymak, J. M., Pinkel, R., Liu, C.-T., Liu, A. K., and David, L.: Prototypical solitons in the South China Sea, Geophys. Res. Lett., 33, L11607, doi:10.1029/2006GL025932, 2006.

Lamb, K. G.: Numerical experiments of internal wave generation by strong tidal flow across a finite amplitude bank edge, J. Geophys. Res., 99, 843–864, 1994.

Lamb, K. G.: A numerical investigation of solitary internal waves with trapped cores formed via shoaling, J. Fluid Mech., 451, 109–144, 2002.

Lamb, K. G.: Shoaling solitary internal waves: on a criterion for the formation of waves with trapped cores, J. Fluid Mech., 478, 81–100, 2003.

Lamb, K. G.: Energy and pseudoenergy flux in the internal wave field generated by tidal flow over topography, Cont. Shelf Res., 27, 1208–1232, doi:10.1016/j.csr.2007.01.020, 2007.

Lamb, K. G.: Internal wave breaking and dissipation mechanisms on the continental slope/shelf, Ann. Rev. Fluid Mech., 46, 231–254, doi:10.1146/annurev-fluid-011212-140701, 2014.

Lamb, K. G. and Nguyen, V. T.: Calculating energy flux in internal solitary waves with an application to reflectance, J. Phys. Oceanogr., 39, 559–580, doi:10.1175/2008JPO3882.1, 2009.

Lamb, K. G. and Wan, B.: Conjugate flows and flat solitary waves for a continuously stratified fluid, Phys. Fluids, 10, 2061–2079, 1998.

Lamb, K. G. and Yan, L.: The evolution of internal wave undular bores: comparisons of a fully nonlinear numerical model with weakly nonlinear theory, J. Phys. Oceanogr., 26, 2712–2734, 1996.

Li, Q. and Farmer, D. M.: The generation and evolution of nonlinear internal waves in the deep basin of the South China Sea, J. Phys. Oceanogr, 41, 1345–1363, doi:10.1175/2011JPO4587.1, 2011.

Lien, R.-C., D'Asaro, E., Henyey, F., Chang, M. H., Tang, T. Y., and Yang, Y. J.: Trapped core formation within a shoaling nonlinear internal wave, J. Phys. Oceanogr., 42, 511–525, doi:10.1175/2011JPO4578.1, 2012.

Lien, R.-C., Henyey, F., Ma, B., and Yang, Y. J.: Large-amplitude internal solitary waves observed in the northern South China Sea: properties and energetics, J. Phys. Oceanogr., 44, 1095–1115, doi:10.1175/JPO-D-13-088.1, 2014.

Liu, A. K., Chang, Y. S., Hsu, M.-K., and Liang, N. K.: Evolution of nonlinear internal waves in the East and South China Seas, J. Geophys. Res., 103, 7995–8008, 1998.

Lynch, J. F., Ramp, S. R., Chiu, C.-S., Tang, T. Y., Yang, Y.-J., and Simmen, J. A.: Research highlights from the Asian Seas International Acoustics Experiment in the South China Sea, IEEE J. Oceanic Eng., 29, 1067–1074, doi:10.1109/JOE.2005.843162, 2004.

Niwa, Y. and Hibiya, T.: Numerical study of the spatial distribution of the M_2 internal tide in the Pacific Ocean, J. Geophys. Res., 106, 22441–22449, 2001.

Niwa, Y. and Hibiya, T.: Three-dimensional numerical simulation of M_2 internal tides in the East China Sea, J. Geophys. Res., 106, C04027, doi:10.1029/2003JC001923, 2004.

Orr, M. H. and Mignerey, P. C.: Nonlinear internal waves in the South China Sea: observation of the conversion of depression internal waves to elevation internal waves, J. Geophys. Res., 108, 3064, doi:10.1029/2001JC001163, 2003.

Osborne, A. R. and Burch, T. L.: Internal solitons in the Andaman Sea, Science, 208, 451–460, 1980.

Ramp, S. R., Tang, T. Y., Duda, T. F., Lynch, J. F., Liu, A. K., Chiu, C.-S., Bahr, F. L., Kim, H.-R., and Yang, Y.-J.: Internal solitons in the northeastern South China Sea, Part I: Sources and deep water propagation, IEEE J. Oceanic Eng., 29, 1157–1181, doi:10.1109/JOE.2004.840839, 2004.

Reeder, D. B., Ma, B. B., and Yang, Y. J.: Very large subaqueous sand dunes on the upper continental slope in the South China Sea generated by episodic, shoaling deep-water internal solitary waves, Mar. Geol., 279, 12–18, doi:10.1016/j.margeo.2010.10.009, 2011.

St. Laurent, L.: Turbulent dissipation on the margins of the South China Sea, Geophys. Res. Lett., 35, L23615, doi:10.1029/2008GL035520, 2008.

Stastna, M. and Lamb, K. G.: Large fully nonlinear internal solitary waves: the effect of background current, Phys. Fluids, 14, 987–2999, 2002.

Vitousek, S. and Fringer, O. B.: Physical vs. numerical dispersion in nonhydrostatic ocean modeling, Ocean Model., 40, 72–86, doi:10.1016/j.ocemod.2011.07.002, 2011.

Vlasenko, V. and Hutter, K.: Numerical experiments on the breaking of solitary internal waves over a slope-shelf topography, J. Phys. Oceanogr., 32, 1779–1793, 2002.

Vlasenko, V. and Stashchuk, N.: Three-dimensional shoaling of large-amplitude internal waves, J. Geophys. Res., 112, C11018, doi:10.1029/2007JC004107, 2007.

Vlasenko, V., Ostrovsky, L., and Hutter, K.: Adiabatic behavior of strongly nonlinear internal solitary waves in slope-shelf areas, J. Geophys. Res., 110, C04006, doi:10.1029/2004JC002705, 2005.

Vlasenko, V., Guo, C., and Stashchuk, N.: On the Mechanism of A-type and B-type internal solitary wave generation in the northern South China Sea, Deep-Sea Res. Pt. I, 69, 100–112, doi:10.1016/j.dsr.2012.07.004, 2012.

Wang, Y.-H., Dai, C.-F., and Chen, Y.-Y..: Physical and ecological processes of internal waves on an isolated reef ecosystem in the South China Sea, Geophys. Res. Lett., 34, L18609, doi:10.1029/2007GL030658, 2007.

Warn-Varnas, A., Hawkins, J., Lamb, K. G., Piacsek, S., Chin-Bing, S., King, D., and Burgos, G.: Solitary wave generation dynamics at Luzon Strait, Ocean Model., 31, 9–27, doi:10.1016/j.ocemod.2009.08.002, 2010.

Yang, Y. J., Tang, T. Y., Chang, M. H., Lui, A. K., Hsu, M.-K., and Ramp, S. R.: Solitons Northeast of Tung-Sha Island during the ASIAEX pilot studies, IEEE J. Oceanic Eng., 29, 1182–1199, doi:10.1109/JOE.2004.841424, 2004.

Yang, Y. J., Fang, Y. C., Chang, M.-H., Ramp, S. R., Kao, C.-C., and Tang, T. Y.: Observations of Second Baroclinic Mode Internal Solitary Waves on the Continental Slope of the Northern South China Sea, J. Geophys. Res., 114, C10003, doi:10.1029/2009JC005318, 2009.

Yang, Y. J., Fang, Y. C., Tang, T. Y., and Ramp, S. R.: Convex and concave types of second baroclinic mode internal solitary waves, Nonlin. Processes Geophys., 17, 605–614, doi:10.5194/npg-17-605-2010, 2010.

Zhao, X. and Alford, M. H.: Source and propagation of internal solitary waves in the northeastern South China Sea, J. Geophys. Res., 111, c11012, doi:10.1029/2006JC003644, 2006.

Table 1. Properties of Initial ISWs in 3000 m depth. $\bar{\rho}$ is the density stratification used, $\bar{E}_a$ and $\bar{E}_k$ are the available potential energy and kinetic energy of the wave, a is the wave amplitude (maximum isopycnal displacement), c the wave propagation speed and U_{max} is the maximum horizontal current in the wave.

$\overline{\rho}$	$\overline{E}_{\mathrm{a}}$ (MJ m^{-1})	$\overline{E}_{\mathrm{k}}$ (MJ m^{-1})	a (m)	c (m s^{-1})	U_{max} (m s^{-1})
$\overline{\rho}_{\mathrm{b}}$	70.0	72.3	35.9	2.53	0.35
–	100.0	104.3	45.4	2.56	0.46
–	150.0	158.6	59.3	2.61	0.62
–	200.0	214.2	71.6	2.64	0.77
–	250.0	271.2	83.1	2.68	0.93
–	300.0	329.7	93.9	2.72	1.11
–	350.0	390.4	104.5	2.76	1.30
–	400.0	454.6	115.2	2.81	1.53
$\overline{\rho}_1$	50.0	51.0	26.29	2.57	0.23
–	100.0	103.2	41.72	2.60	0.38
–	150.0	156.6	54.70	2.64	0.53
$\overline{\rho}_2$	50.0	50.8	26.20	2.51	0.20
–	100.0	102.6	41.43	2.54	0.32
–	150.0	155.3	54.11	2.56	0.43

Table 2. Shoaling cases starting at 3000 m depth. Cases run using bathymetry h_{15} without the bump are indicated with an optional nb and cases run with rotation turned on are indicated by an optional r. Three sets of simulations were run with and without viscosity. These are indicated by the (ν). Cases numbers with an optional ν indicate cases run with viscosity. For these cases three values of ν were used, the value of ν being indicated by a number, e.g., νn where values of $n = 3$, 4, or 5 are for $K = 10^{-n}\,\mathrm{m^2\,s^{-1}}$. Thus Case 4nb was run with the bump removed and Case 4_r was the same as Case 4 but with rotation turned on. Case 9ν4 was run with a viscosity using $K = 10^{-4}\,\mathrm{m^2\,s^{-1}}$.

Case	ρ	$\overline{E}_\mathrm{a}$ (MJ m^{-1})	a (m)	Bathymetry
1	ρ_b	50	28.7	h_0
2	–	100	45.4	–
3(r)	–	100	–	h_{15}
4(nb)_(r)	–	150	59.3	–
5(r)	–	200	71.6	–
6(r)	–	250	83.1	–
7(r)	–	400	115.3	–
8(r) (ν)	ρ_1	50	26.3	–
9(ν)	–	100	41.7	–
10(ν)	–	150	54.7	–
11(r)	ρ_2	50	26.2	–
12	–	100	41.4	–
13	–	150	54.1	–

Table 3. Maximum increase in wave amplitude of ISW solutions of the DJL equation. First column is total energy (available potential and kinetic energy). a_{3000} is the wave amplitude in a water depth of 3000 m. $\max a$ is the maximum wave amplitude for the given energy, $d_{\max}$ is the water depth where the maximum occurs. The three values separated by / are values for densities $\overline{\rho}_{\mathrm{b}}$, $\overline{\rho}_1$ and $\overline{\rho}_2$. Given values are based on DJL solutions calculated at depth intervals of 50 m (see Fig. 11).

$\overline{E}$ (MJ m^{-1})	a_{3000} (m)	$\max a$ (m)	$\frac{\max a}{a_{3000}}$	$d_{\max}$ (m)
50	18/16/18	62/56/70	3.4/3.4/4.2	250/300/250
100	28/28/26	81/74/89	2.9/2.8/3.4	300/350/300
200	45/41/41	105/98/113	2.3/2.4/2.7	400/400/350
400	70/65/64	134/127/142	1.9/2.0/2.2	450/500/450
600	91/85/84	154/147/162	1.7/1.7/1.9	500/600/500
1000	129/120/116	183/178/191	1.4/1.4/1.6	600/600/600

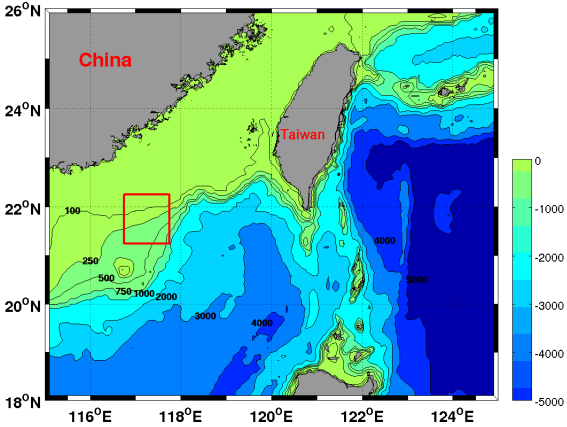

Figure 1. Luzon Strait and South China Sea region. Red square is location of ASIAEX experimental site. Colours show depth in meters.

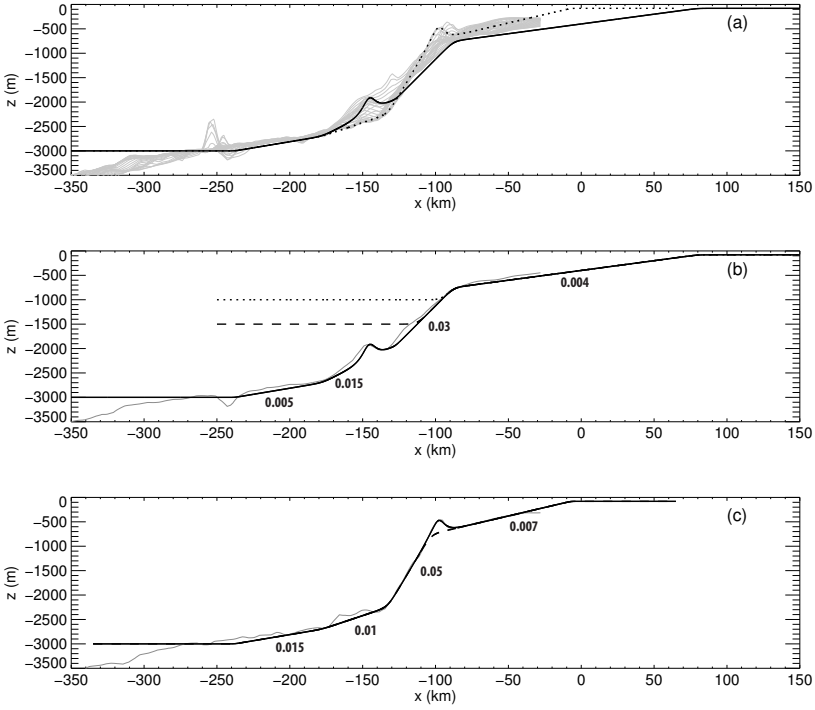
(a)
(b)
(c)
z (m)
x (km)
0.004
0.03
0.015
0.005
0.007
0.05
0.01
0.015

Figure 2. Sample measured bathymetries at the ASIAEX location extracted from the Digital Bathymetry 2 min resolution (DB2) data base inside the red square area in Fig. 1. **(a)** Comparison of 24 different measured bathymetries (grey) with two model bathymetry (solid and dotted black curves). **(b)** Comparison of first model bathymetry, h_0, (black) with one of the measured bathymetries (grey). The bathymetries used for simulations starting at depths of 1000 and 1500 m are also shown. **(c)** Comparison of two other model bathymetries (solid and dashed black curves) with a second measured bathymetry (grey). The solid curve is bathymetry h_{15}. The dashed curved is the same bathymetry with the bump at -100 km removed. In panels (**b**,**c**) slopes of parts of the bathymetry are indicated.

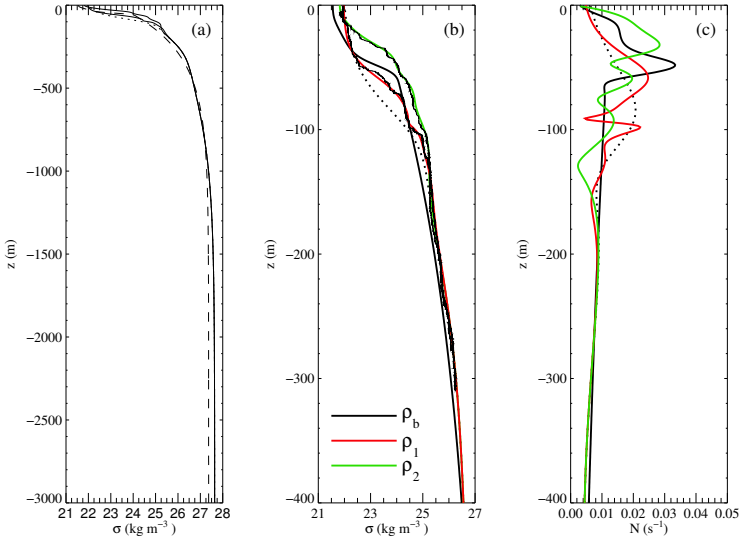

Figure 3. Stratifications. **(a)** ~~$\sigma = \rho - 1000$~~ $\sigma_\theta = \rho - 1000$ kg m^{-3} for the base stratification (dashed) and two fits to observed stratifications (solid). Lower solid curve is $\overline{\rho}_1$. Upper solid curve is $\overline{\rho}_2$. For comparison the dotted line is the Luzon Strait stratification used in Warn-Varnas et al. (2010). **(b)** Stratifications in upper 400 m. Base stratification (thick black curve), $\overline{\rho}_1$ (red), $\overline{\rho}_2$ (green) and Luzon Strait stratification (dotted). Thin solid lines show corresponding observed density profile. **(c)** N (rad s^{-1}) for model stratifications shown in **(b)**.

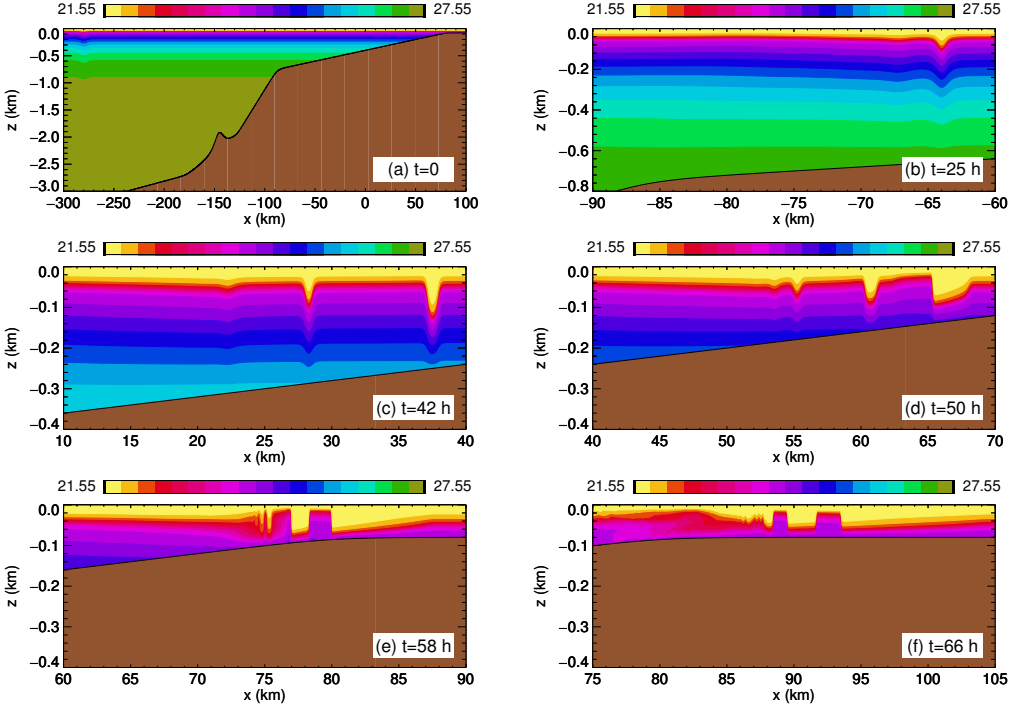

Figure 4. Density fields for Case 2 using bathymetry h_0. Resolution: $\Delta x = 33\,\mathrm{m}$, $J = 400$. Initial wave amplitude 45 m. **(a)** 0 h (full depth shown). **(b)** 25 h. **(c)** 42 h. **(d)** 50 h. **(e)** 58 h. **(f)** 66 h. The initial wave at $x = -280\,\mathrm{km}$ is barely detectable at this scale. Panel (a) shows the full depth, panel (b) the upper 800 m and the remainder the upper 400 m of the water column. Density values are σ σ_θ in $\mathrm{kg\,m^{-3}}$.

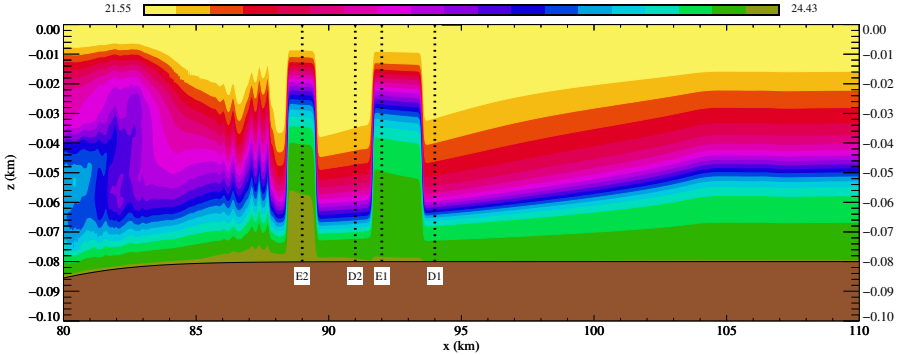

Figure 5. Close up of shoaling waves from Case 2 at $t = 66\,\mathrm{h}$ shown in Fig. 4f showing onset of breaking behind the leading two waves. Vertical dashed lines are locations of vertical profiles shown in Fig. 6.

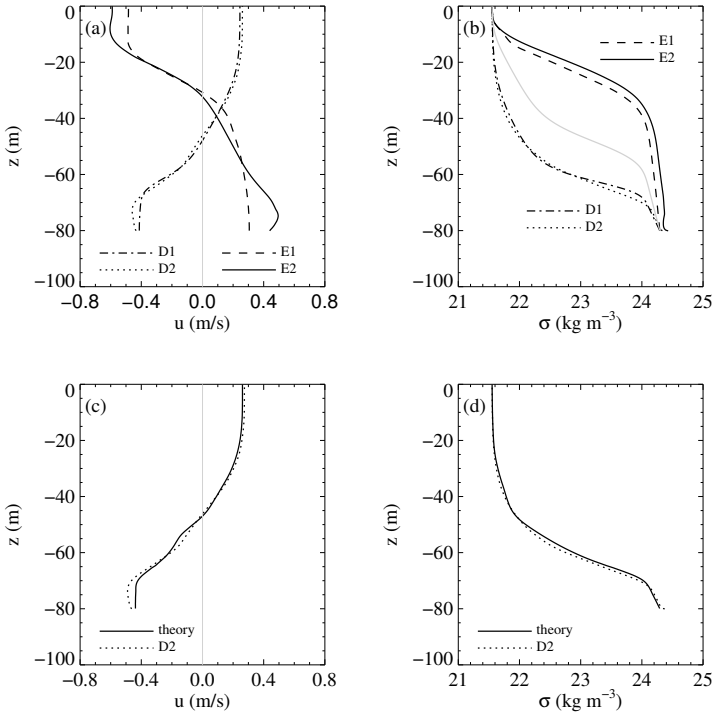

Figure 6. (a, b) Vertical profiles of horizontal velocity and density for Case 2 at $t = 66$ h at locations shown in Fig. 5. **(a)** Horizontal velocity. **(b)** Density. Curves from second wave pedestal at $x = 89$ km (solid), the second depression at $x = 91$ km (dots), the first pedestal at $x = 92$ km (dashed), and in the leading depression at $x = 94$ km (dash-dot) (see Fig. 5 for profile locations). The light grey curve in **(b)** shows the background density profile. **(c, d)** Profiles in solitary waves of depression (solid) computed on background field given by profiles extracted from simulation in the pedestal at $x = 92$ km between the two leading waves of depression. Solution is compared with profiles taken from the second depression at $x = 91$ km (dots).

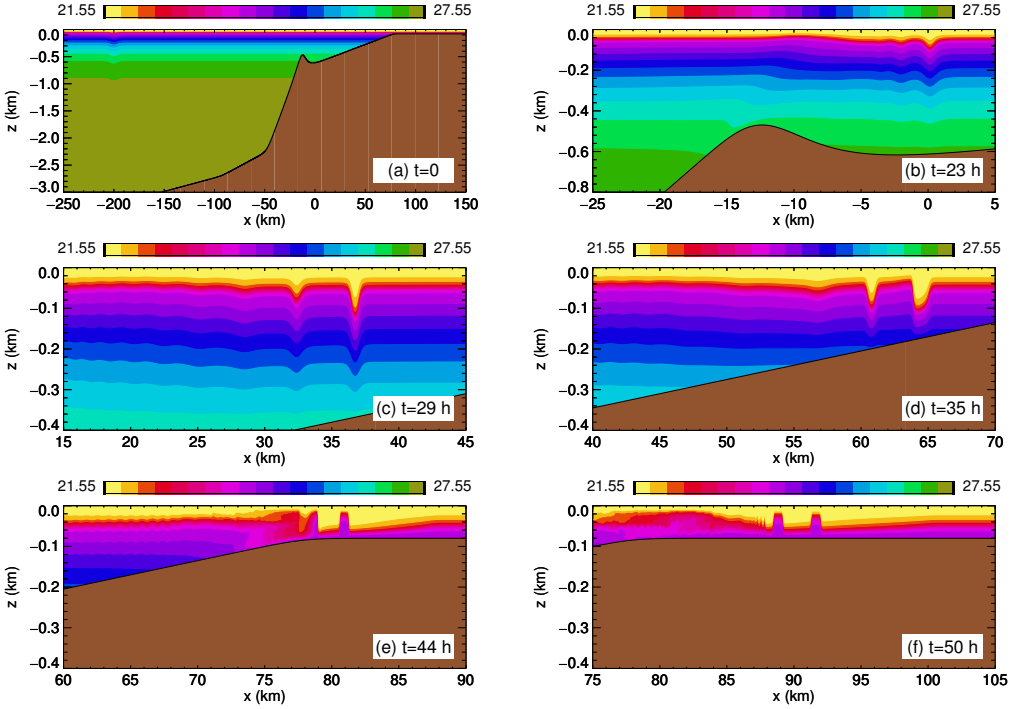

Figure 7. Density fields for Case 3 using bathymetry h_{15} and stratification $\overline{\rho}_{\mathrm{b}}$. Resolution: $\Delta x = 33\,\mathrm{m}$, $J = 400$. Initial wave amplitude 45 m, (APE $= 100\,\mathrm{MJ\,m^{-1}}$). **(a)** 0 h. **(b)** 23 h. **(c)** 29 h. **(d)** 35 h. **(e)** 44 h. **(f)** 50 h.

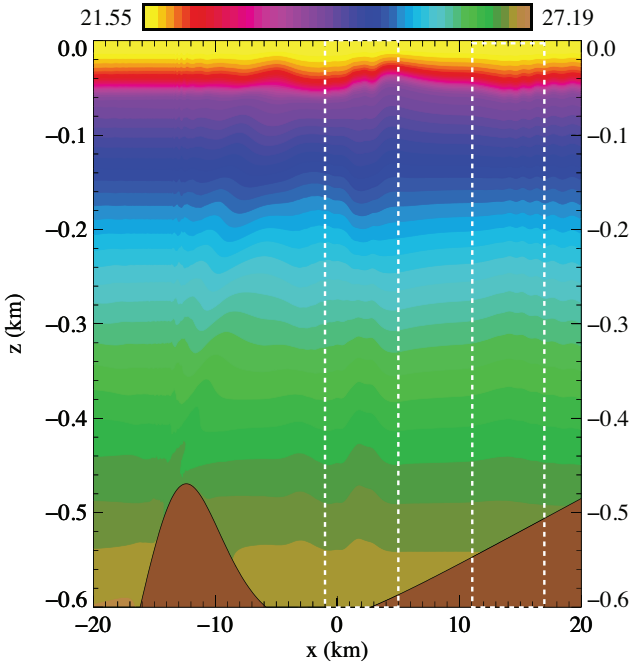

Figure 8. Density field for same case and time shown in Fig. 7c showing mode-two waves (in white dashed boxes) and an internal wave beam (above the bump) generated when the solitary wave passes over the bump.

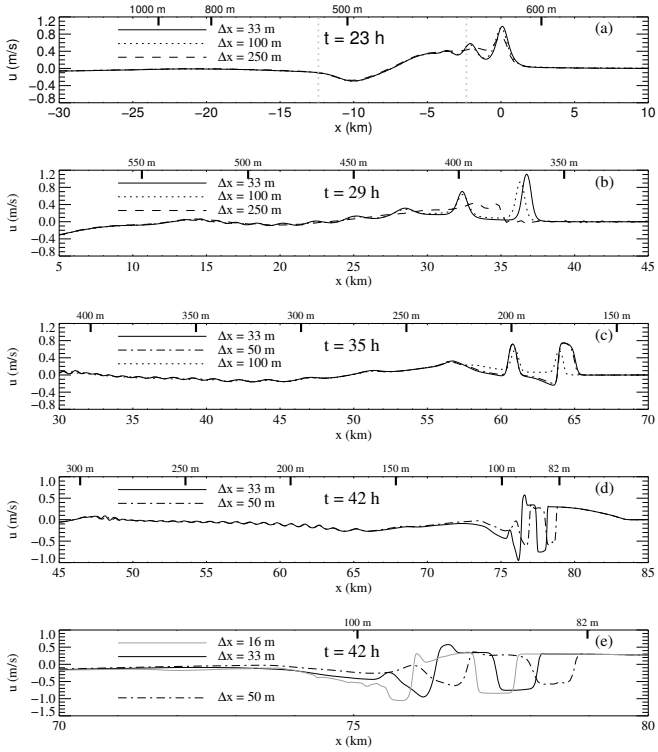

Figure 9. Resolution test results. Shown are surface currents at four different depths for Case 3 which uses bathymetry h_{15} and an initial wave amplitude of 45 m. Panels compare results from simulations with different horizontal resolutions using 200 grid points in the vertical. Leading wave at 610 m depth – see Fig. 7b. **(b)** $t = 29$ h. Leading wave at 370 m depth – see Fig. 7c. **(c)** $t =$ 35 h. Leading wave at 180 m depth – see Fig. 7d. **(d)** Results at $t = 42$ h. First depression in water shallower than 82 m. Second depression at 90 m depth. **(e)** Zoom in on leading waves at $t = 42$ h. Vertical dashed lines in panel (a) indicate the location of the crest of bump and the depth maximum between the bump and the shelf. Depths are indicated by black marks along upper axis.

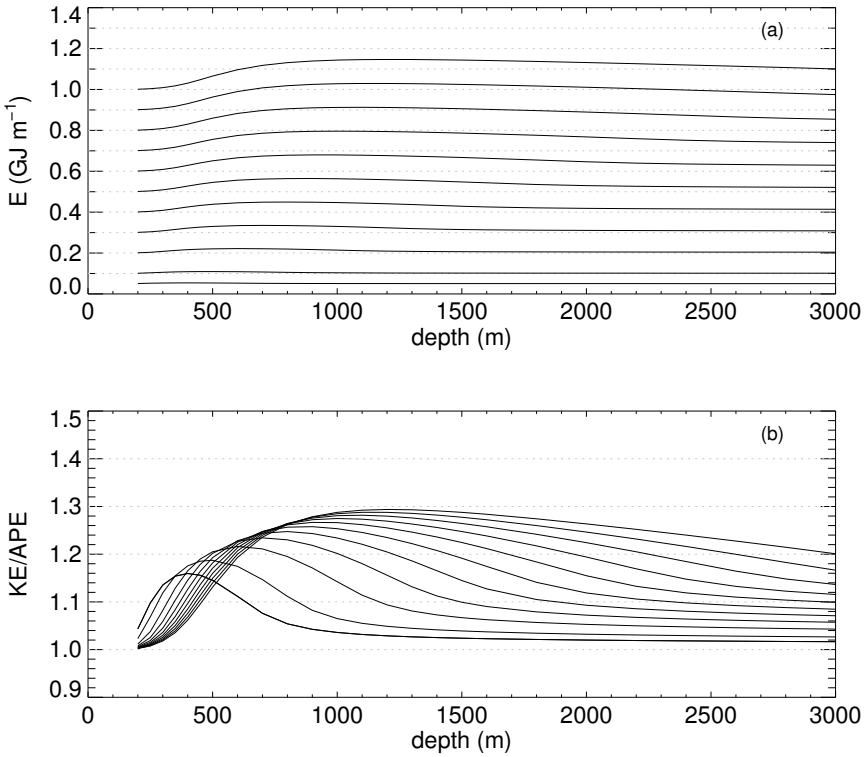

Figure 10. (a) Total ISW energy (APE plus KE) for ISWs with fixed APE as a function of water depth. Curves are for APE equal to 25 MJ m^{-1} and 50 MJ m^{-1} to 500 MJ m^{-1} in increments of 50 MJ m^{-1}. **(b)** Ratio of KE to APE for same waves. On right side the ratio increases with APE.

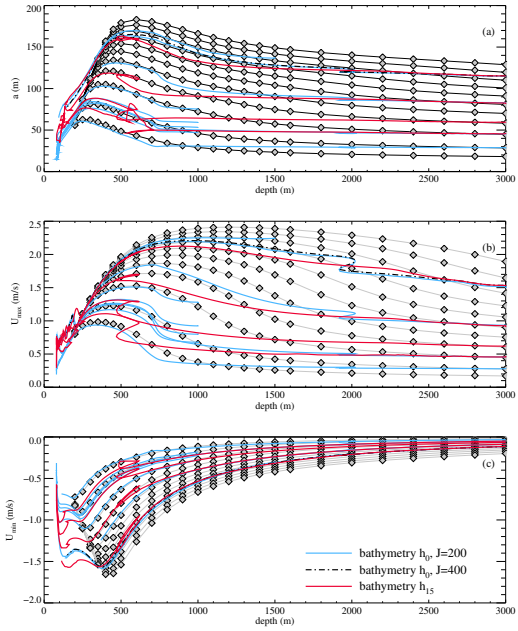

Figure 11. Wave properties as a function of water depth. **(a)** Wave amplitudes (absolute value), **(b)** maximum surface currents, **(c)** minimum bottom currents. Grey curves with diamonds are for ISW solutions of the DJL equation for waves with total energy E equal to 50 MJ m^{-1} and 100 to 1000 MJ m^{-1} in increments of 100 MJ m^{-1}. Diamonds indicate computed values. Coloured curves are maximum absolute amplitude and surface current and minimum bottom currents of shoaling waves as function of water depth. Blue – cases using bathymetry h_0. Red – cases using bathymetry h_{15}. Black dash-dot – higher resolution case using bathymetry h_0. This curve overlies the lower resolution result (blue curve, initial amplitude 115 m). Both are overlain by the results using bathymetry h_{15} for depths greater than about 2600 m.

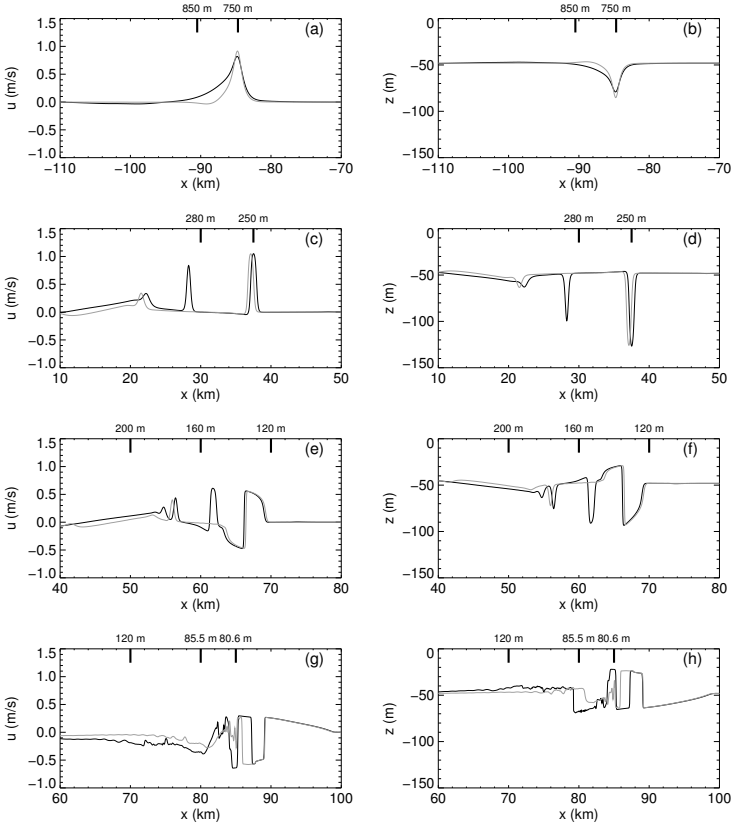

Figure 12. Surface current (left) and ~~$\sigma_t = 0.0232$~~$\sigma_\theta = 23.2$ kg m^{-3} isopycnal (right) at different times for waves with initial APE of 100 and 60 MJ m^{-1} started at depths of 3000 (solid) and 1000 m (dashed) respectively using bathymetry h_0. Times are different for the two waves, chosen so that the leading waves are at approximately the same location. Sample local depths are indicated along the upper axis.

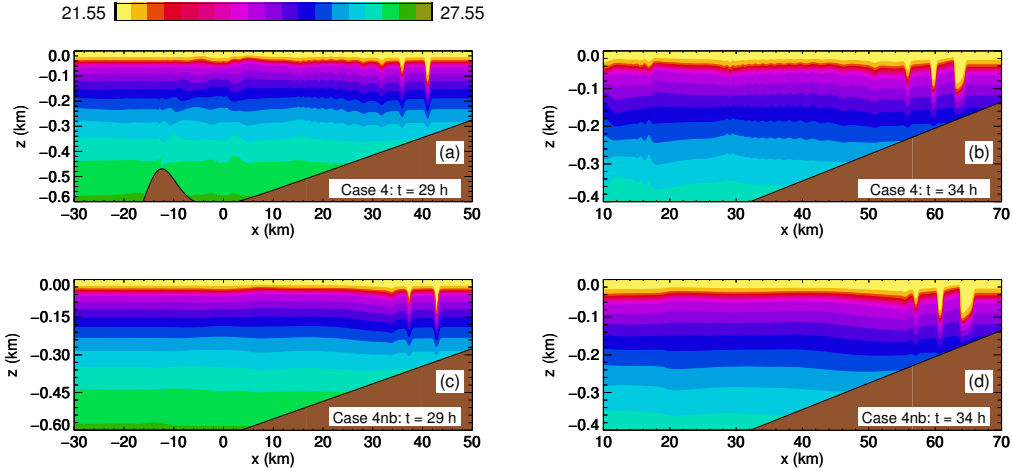

Figure 13. Effects of the bump for bathymetry h_{15}. Initial amplitude 59 m (Cases 4 and 4nb). **(a, b)** Bathymetry h_{15}. **(c, d)** Bathymetry h_{15} with bump removed.

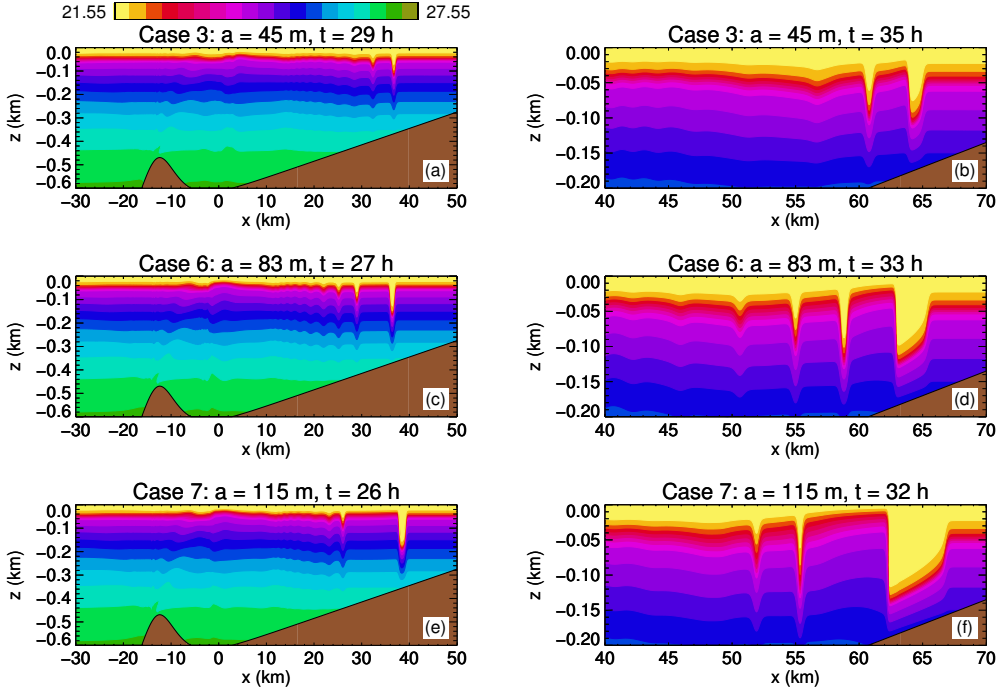

Figure 14. Density fields for shoaling waves with different initial wave amplitudes using bathymetry h_{15} and stratification $\overline{\rho}_{\mathrm{b}}$.

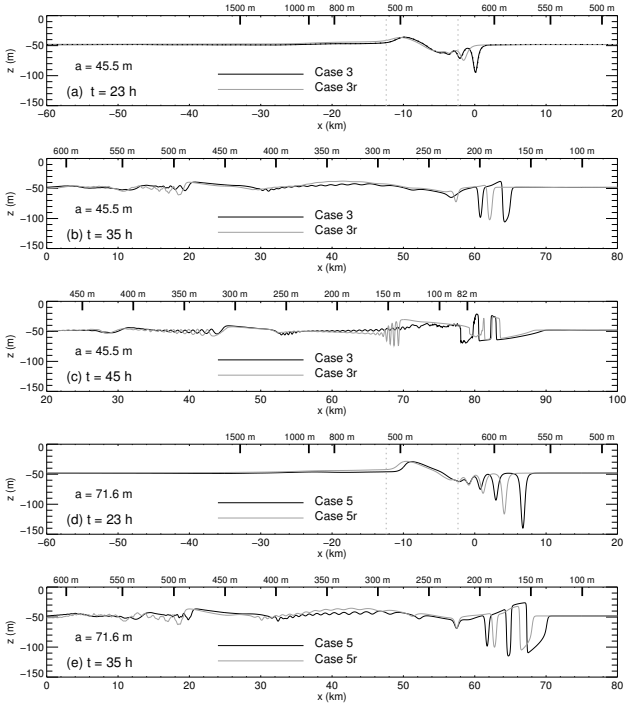

Figure 15. Effects of rotation are illustrated by comparing the ~~$\sigma_t = 0.0232$~~ $\sigma_\theta = 23.2$ kg m^{-3} isopycnals for two different initial waves. Base stratification with bathymetry h_{15}. **(a, b, c)** Cases 3 and 3r: initial wave amplitude is 45.4 m (APE $= 100$ MJ m^{-1}). **(d, e)** Cases 5 and 5r: initial wave amplitude is 71.6 m (APE $= 200$ MJ m^{-1}). Solid black curves are results without rotational effects. Solid grey curves are results with $f = 5.35 \times 10^{-5}$ s^{-1}. Vertical dashed lines indicate the location of the crest of bump and the depth maximum between the bump and the shelf. Depths are indicated by black marks along upper axis.

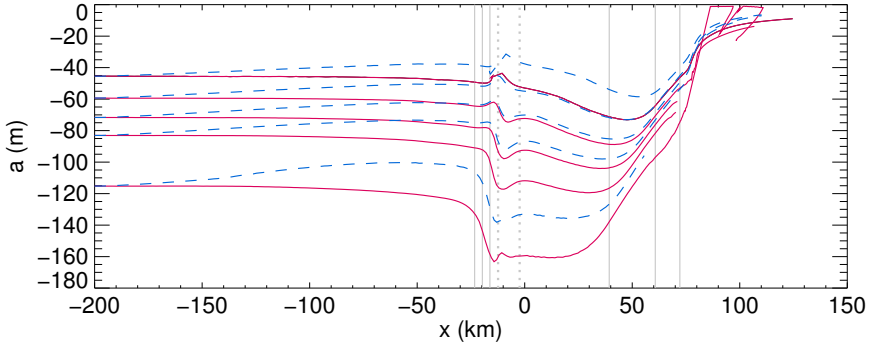

Figure 16. Effects of rotation on the amplitude of the leading wave as a function of x. Bathymetry h_{15}. Solid red curves: cases without rotation. Dashed blue curves: cases with rotation. Cases 3–7 and 3r–7r. The solid vertical grey lines indicate locations where water depth is 1000, 800, 600 (first occurrence), 350, 200 and 120 m. The vertical dashed lines indicate the locations of the top of the bump at $x = -12.4$ km (480 m depth) and maximum depth (618 m) up shelf of it.

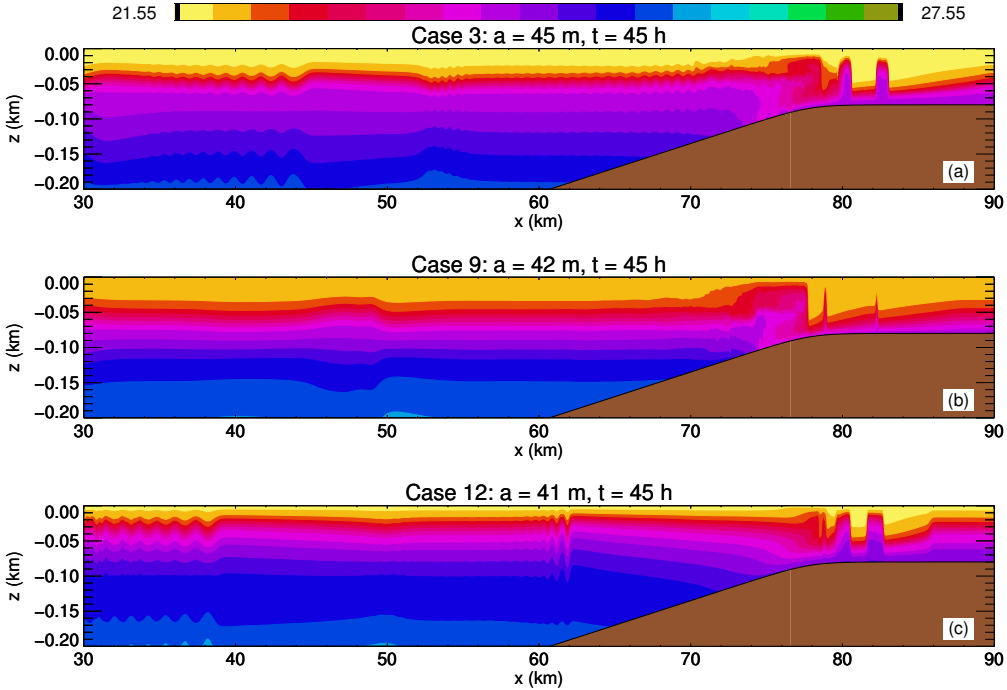

Figure 17. Comparisons of wave fields using observed stratifications for APE $= 100\,\mathrm{MJ\,m^{-1}}$ and bathymetry h_{15}. $f = 0$. **(a)** Case 8: density $\overline{\rho}_b$. **(b)** Case 9: density $\overline{\rho}_1$. **(c)** Case 12: density $\overline{\rho}_2$.

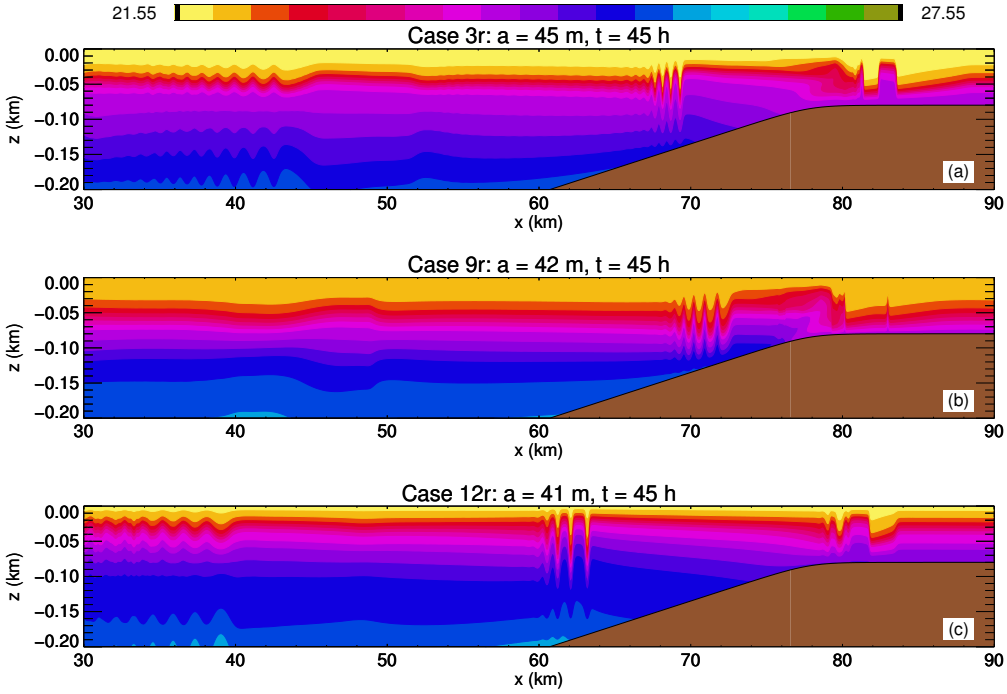

Figure 18. Same as previous figure but with $f = 5.33 \times 10^{-5}\,\mathrm{s}^{-1}$.

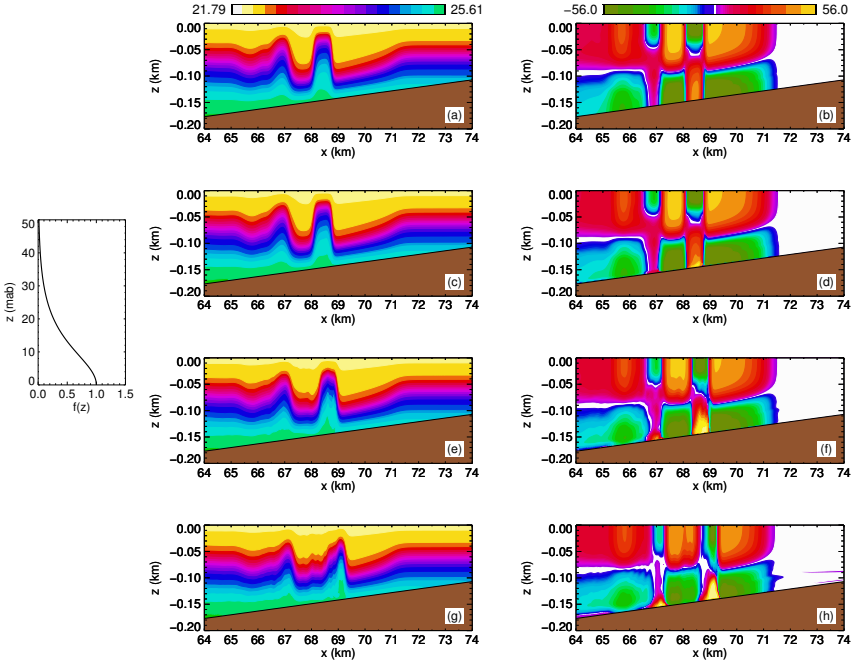

Figure 19. Effects of viscosity on shoaling waves. Stratification $\overline{\rho}_1$, initial wave amplitude 41.7 m (APE $= 100\,\mathrm{MJ\,m^{-1}}$). Left column shows the density field (σ_θ), right column shows the corresponding horizontal velocity (in $\mathrm{cm\,s^{-1}}$). For the velocity fields the red-orange-yellow colours indicate positive (on shelf) currents while green-blue indicate negative currents. Left inset shows the eddy visocity/diffusivity profile function $f(z - z_b)$. **(a, b)** Inviscid. **(c, d)** $K = 1.0 \times 10^{-5}\,\mathrm{m^2\,s^{-1}}$. **(e, f)** $K = 1.0 \times 10^{-4}\,\mathrm{m^2\,s^{-1}}$. **(g, h)** $K = 1.0 \times 10^{-3}\,\mathrm{m^2\,s^{-1}}$.